Unified Description and Optimization Method of Dual Active Bridge DC–DC Converters

Ziheng Xiao, *Student Member, IEEE*, Zhixing He, *Member, IEEE*, Zongjian Li, *Member, IEEE*, Lipeng Zhu, *Member, IEEE*, and Lei Wang, *Senior Member, IEEE*

***Abstract*—The optimization of dual active bridge converters (DAB) is widely studied and numerous modulation schemes are proposed to enhance the performance of a DAB converter. However, a unified description method both suitable for time and frequency domain analysis still lacks. Besides, the optimization process encounters a difficulty of the potential nonconvex feasible region restricted by the power transmission equality, making the regular convex optimization methods no longer applicable. To solve these problems, this article gave a unified description method both suitable for time and frequency domain analysis based on the standard decomposition of instantaneous electric quantities. Besides, a unified optimization method is proposed based on tangent point searching for the feasible region and optimization objective surfaces. With the proposed unified optimization method, the optimization objective can be designed arbitrarily as long as it is piecewise continuous, and smooth. An efficiency-oriented optimization objective design method is introduced considering all electric quantities as well as the soft-switching conditions. Finally, the experimental results confirm the unified optimization method and the efficiency-oriented optimization objective design method.**

***Index Terms*—Dual active bridge converter (DAB), efficiency-oriented optimization objective design method, unified optimization method.**

NOMENCLATURE

Abbreviations

DAB	Dual active bridge.
SST	Solid-state transformer.
HFT	High-frequency transformer.
SPS	Single-phase shift.
DPS	Dual-phase shift.
EPS	Extended phase shift.
rms	root mean square.
KKT	Karush–Kuhn–Tucker.
LMM	Lagrange multiplier method.
CCT	Control coordinate trajectories.
EF	Exit flag.
ZVS	Zero voltage switching.
iZVS	Insufficient zero voltage switching.
HS	Hard switching.

Symbols

L	Power transmission inductor of DAB.
n	Turn ratio of the HFT.
f_{s}	Switching frequency of DAB.
M	Voltage gain of DAB.
v_{AB}	Voltage of output port AB.
v_{CD}	Voltage of output port CD.
i_{L}	Inductor current of DAB.
α	Phase shift angle between two bridges.
φ_1	Duty ratio in primary bridge.
φ_2	Duty ratio in secondary bridge.
$\mathbf{X}$	Control coordinate (α, φ_1, φ_2).
V_{in}	Input voltage of DAB.
V_{o}	Output voltage of DAB.
I_{Peak}	Peak inductor current of DAB.
I_{rms}	RMS inductor current of DAB.
V_{rms}	RMS inductor voltage of DAB.
P_{SW}	Switching loss of DAB.
P_{Ohm}	Ohmic loss of DAB.
P_{Cond}	Conduction loss of DAB.
P_{Loss}	Overall power loss of DAB.
P_{Iron}	Iron loss of DAB.
$P_{\mathrm{Iron\text{-}L}}$, $P_{\mathrm{Iron\text{-}T}}$	Iron loss of L and HFT.
P_{Unkn}	Unknown loss of DAB.
P_{VL}, P_{VT}	Core loss densities of L and HFT.
V_{eL}, V_{eT}	Core volumes of L and HFT.
B_{Lm}, B_{Tm}	Peak magnetic flux density of L and HFT.
k_{L}, α_{L}, β_{L}	Steinmetz parameters of L.
k_{T}, α_{T}, β_{T}	Steinmetz parameters of HFT.
N_{T}, N_{L}	Winding turns of L and HFT.
A_{cT}, A_{cL}	Effective core cross section of L and HFT.
K_{A}, K_{L}, K_{T}	Optimization coefficients of P_{Iron}.
K_{SW}, K_{Cond}	Optimization coefficients of P_{SW}, P_{Cond}.
$S(\theta)$, $T(\theta)$	Square/ triangular wave functions.
θ_{a}, θ_{b}, θ_{c}, θ_{d}	Four changing points of DAB.
$v(\theta_1, \theta_2)$	Basic voltage function of DAB.
$i(\theta_1, \theta_2)$	Basic current function of DAB.
$p(\theta_1, \theta_2)$	Basic power function of DAB.
$p_{\mathrm{AB}}(\theta)$	Instantaneous power of port AB.

Manuscript received October 23, 2021; revised January 28, 2022 and April 19, 2022; accepted May 19, 2022. Date of publication May 23, 2022; date of current version June 24, 2022. This work was supported in part by the Outstanding Youth Fund of Hunan Province under Grant 2021JJ20014 and in part by the National Natural Science Foundation of China under Grants 52177180 and 52107193. Recommended for publication by Associate Editor M. Amirabadi. *(Corresponding author: Zongjian Li.)*

The authors are with the College of Electrical and Information Engineering, Hunan University, Changsha 410082, China (e-mail: zihengxiao@hnu.edu.cn; hezhixing@hnu.edu.cn; lzjq1@hnu.edu.cn; lpzhu@hnu.edu.cn; jordanwanglei@hnu.edu.cn).

Color versions of one or more figures in this article are available at https://doi.org/10.1109/TPEL.2022.3177245.

Digital Object Identifier 10.1109/TPEL.2022.3177245

$p_{\mathrm{CD}}(\theta)$	Instantaneous power of port CD.
P, P_{AB}, P_{CD}	Normalized average power of DAB.
S_{AB}, S_{CD}	Apparent power of port AB and port CD.
$v_{\mathrm{ABs}}(n)$, $v_{\mathrm{ABc}}(n)$	nth sine and cosine coefficient of v_{AB}.
$v_{\mathrm{CDs}}(n)$, $v_{\mathrm{CDc}}(n)$	nth sine and cosine coefficient of v_{CD}.
$i_{\mathrm{Ls}}(n)$, $i_{\mathrm{Lc}}(n)$	nth sine and cosine coefficient of i_{L}.
$p_{\mathrm{ABs}}(n)$, $p_{\mathrm{ABc}}(n)$	nth sine and cosine coefficient of p_{AB}.
$p_{\mathrm{CDs}}(n)$, $p_{\mathrm{CDc}}(n)$	nth sine and cosine coefficient of p_{CD}.
$A(\mathbf{X})$	Optimization objective of DAB.
$P(\mathbf{X})$	Equality power constraint of DAB.
$B_{\mathrm{i}}(\mathbf{X})$	Feasible region restraints of DAB.
$\boldsymbol{C}(\mathbf{X})$	Optimal control coordinate table.
$\boldsymbol{n_{\mathrm{P}}}$, $\boldsymbol{n_{\mathrm{A}}}$	Normal vectors of $P(\mathbf{X})$ and $A(\mathbf{X})$.
$\mathbf{X}_{\mathrm{opt}}$	Optimal control coordinate.
$\mathbf{X_{opt\text{-}B}}$, $\mathbf{X_{opt\text{-}i}}$	Two calculated optimal control coordinate.
$H_{\mathrm{A}}(\mathbf{X})$	Hessian matrix of the control coordinate.
$\lvert Q_{\mathrm{AB}}\rvert$, $\lvert Q_{\mathrm{CD}}\rvert$	Reactive power of port AB and port CD.
I_{P}, I_{N}	Normalized minimum ZVS currents.

I. Introduction

DUAL active bridge (DAB) attracts more and more attention in the academic cycle as well as industry cycle due to the advantage of galvanic isolation, bidirectional buck and boost operation capability, intrinsic soft-switching characteristic, and high power density.

DAB are widely adopted in dc microgrid [1]–[4], automotive application [5], [6], distribution system [7], and the isolation stage in solid-state transformers (SSTs) [8]–[12]. The DAB is depicted in Fig. 1(a), where a DAB consists of four primary switches, four secondary switches, an high-frequency transformer (HFT), and a power transmission inductor L. The turn ratio of the HFT is 1:n and the switching frequency is f_{s}. With the switching of primary and secondary switches, the output port of AB and CD generate two three-level square wave v_{AB} and v_{CD}, and the inductor current i_{L} is piecewise linear with different slopes. By controlling the sequences of the switches, the power transmission can be positive (from primary to secondary), or negative (from secondary to primary).

The operation waveforms of DAB are depicted in Fig. 1(b). The phase shift angle between two bridges α, duty ratios in primary bridge φ_1 and in secondary bridge φ_2 are expressed in radian and the control coordinate is expressed as $\mathbf{X} = (\alpha, \varphi_1, \varphi_2)$. α is measured from the rising edge of v_{AB} to the rising edge of v_{CD}. The range of α, φ_1, and φ_2 are $\alpha \in [\pi, \pi]$, $\varphi_1 \in [0, \pi]$, and $\varphi_2 \in [0, \pi]$, respectively.

Numerous modulation schemes are proposed for the sake of increasing the efficiency and power density of DAB. The SPS was first presented in [13] and [14], and was widely applied due to simple implementation. Moreover, high efficiency can be achieved at rated power when $nV_{\mathrm{in}} \approx V_{\mathrm{o}}$ [15]. However, in low power range or when $nV_{\mathrm{in}} >> V_{\mathrm{o}}$ or $nV_{\mathrm{in}} << V_{\mathrm{o}}$, SPS is with low efficiency and limited soft-switching range [16]. In order to enhance the performance of DAB, dual-phase shift (DPS) was proposed in [17] and further improved in [18] and [19] to eliminate reactive power of DAB with $\varphi_1 = \varphi_2$, which shows good performance in the low power range. EPS was proposed

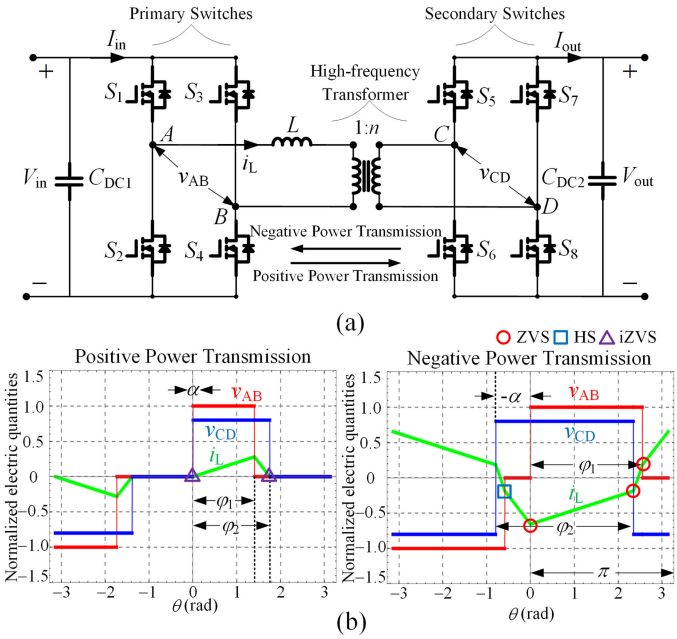

Fig. 1. (a) Topology of DAB. (b) Operating waveforms of DAB with positive and negative power transmission, where the switches with ZVS, hard switching (HS), and incomplete ZVS (iZVS) are denoted in red circle, blue square, and purple triangle.

in [20] to reduce circulating or backflow power with $\varphi_1 = \pi$ or $\varphi_2 = \pi$. A minimum backflow power modulation scheme is proposed in [21] with EPS in SST application. The above-mentioned modulation schemes were based on the characteristic of control coordinate and provided guidance on the control method. However, only local optimum can be obtained due to the additional constraint with DPS and EPS. Therefore, the performance of DAB was not globally optimized. As for DAB, both time and frequency domain electric quantities can be chosen as an optimization objective. In time domain, Gu *et al.* [22], Huang *et al.* [23], and Xiao *et al.* [24] focused on the peak current I_{Peak} to reduce the current stress of switches and proposed multiple modulation schemes with reduced I_{Peak} to reduce the switching losses P_{SW}. Schibli [25], Krismer and Kolar [26], and Tong *et al.* [27] gave a comprehensive analysis of DAB with the minimum root mean square (rms) value of inductor current I_{rms} to reduce the ohmic loss P_{Ohm}. To avoid the operating mode classification in time domain, the frequency domain analysis of DAB is required. A fundamental duty modulation is proposed in [28], which chose the amplitude of the fundamental component of i_{L} as the optimization objective. A maximum fundamental active power modulation scheme is proposed in [29]. However, only fundamental component is considered in [28] and [29] to keep the expressions simple, which resulted in errors in the estimation of electric quantities. If more harmonic components are considered, the accuracy increases but the simplicity is lost.

Generally speaking, the optimization of DAB is faced with the following two difficulties.

1) The time domain electric quantities are piecewise polynomial functions while the frequency domain electric quantities are trigonometric functions. The time domain

TABLE I
ABBREVIATIONS AND NORMALIZATIONS

Variable	Symbol	Normalized variable
Voltage Base	$V_{\text{Base}} = V_{\text{in}}$	-
Impedance Base	$Z_{\text{Base}} = 2\pi f_s L$	-
Time/Duration	t	$\theta = 2\pi f_s t$
Voltage gain	$M = V_o/nV_{\text{in}}$	-
Power Base	$P_{\text{Base}} = M\pi/4$	-

feasible region may be nonconvex under the equality constraint condition of power transmission, and the trigonometric functions are nonconvex. Hence, regular convex optimization methods like Lagrange multiplier method or Karush–Kuhn–Tucker conditions are ineffective [27].

2) The overall power loss of a DAB P_{Loss}, is classified into the iron loss P_{Iron}, the ohmic loss P_{Ohm}, and the switching loss P_{SW}. The efficiency of DAB is related to multiple factors, including I_{Peak}, I_{rms}, and zero voltage switching (ZVS) of the switches. When the optimization objective is solely selected as I_{Peak} or I_{rms}, the highest efficiency cannot be guaranteed in the whole operation range.

To solve the abovementioned difficulties, a unified description method of DAB both suitable for time and frequency domain analysis is established based on the standard decomposition of electric quantities. Besides, a unified optimization method is proposed to minimize an arbitrary optimization objective with equality and inequality constraints.

The rest of this article is organized as follows. The unified description method of DAB is introduced in Section II, and the unified optimization method of DAB is introduced in Section III. In Section IV, some tips and examples of optimization are introduced to verify the proposed unified optimization method. A universal numerical solution for an arbitrary continuous optimization objective and an efficiency-oriented optimization objective design method are also introduced. The experimental results are presented in Section V. Finally, Section VI concludes this article.

II. Unified Description Method of DAB

A unified description method both suitable in time and frequency domain is introduced in this section. To simplify the analysis, normalized values are used and the base values are summarized in Table I.

A. Time Domain Analysis

Apart from the conventional piecewise function method, the description of v_{AB} and v_{CD} are based on the decomposition of the instantaneous voltage and current waveforms. First of all, standard square wave function $S(\theta)$ and triangular wave function $T(\theta)$ with 2π as the minimum period are defined as

$$S(\theta) = \operatorname{sgn}(\sin(\theta)), T(\theta) = -\arcsin(\cos(\theta)). \quad (1)$$

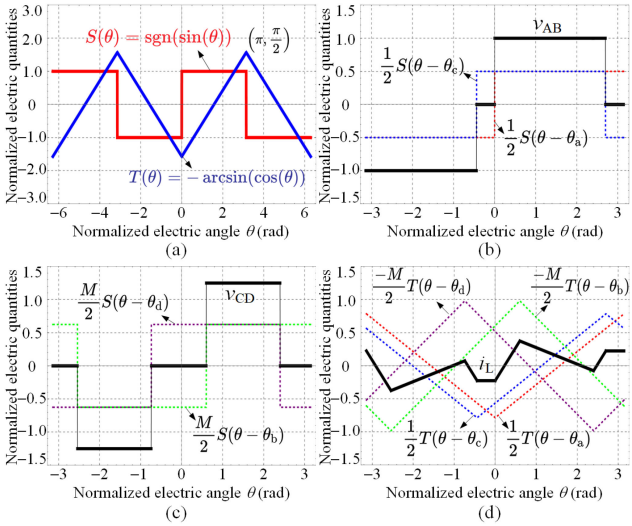

Fig. 2. (a) Waveforms of $S(\theta)$ and $T(\theta)$. (b) Typical waveforms of $v_{\text{AB}}(\theta)$ constructed by two standard square waves. (c) Typical waveforms of $v_{\text{CD}}(\theta)$ constructed by two standard square waves. (d) Typical waveforms of $i_{\text{L}}(\theta)$ constructed by four standard triangular waves.

With this definition, the following relations can be obtained:

$$\int_0^{2\pi} S(\theta) = 0; \int_0^{2\pi} T(\theta) = 0; S(\theta) = \frac{dT(\theta)}{d\theta}; T(\theta) = \int_0^{\theta} S(\theta)\, d\theta. \quad (2)$$

The waveforms of $S(\theta)$ and $T(\theta)$ are depicted in Fig. 2(a). With the control coordinate $(\alpha, \varphi_1, \varphi_2)$, the four changing points of $v_{\text{AB}}(\theta)$, $v_{\text{CD}}(\theta)$, $v_{\text{L}}(\theta)$, and $i_{\text{L}}(\theta)$ are denoted as θ_{a}, θ_{b}, θ_{c}, and θ_{d}, respectively, where

$$\theta_{\text{a}} = 0; \theta_{\text{b}} = \alpha; \theta_{\text{c}} = \varphi_1 - \pi; \theta_{\text{d}} = \varphi_2 + \alpha - \pi. \quad (3)$$

An example of $M = 1.25$, $(\alpha, \varphi_1, \varphi_2) = (0.6, 2.7, 1.8)$ is used to illustrate how the waveforms are constructed, and the typical waveforms are depicted from Fig. 2(b)–(d). In this case, there is $\theta_{\text{a}} = 0$, $\theta_{\text{b}} = 0.6$, $\theta_{\text{c}} = -0.44$, $\theta_{\text{d}} = -0.74$. $v_{\text{AB}}(\theta)$ and $v_{\text{CD}}(\theta)$ are three-level square waveforms, which can be constructed by two standard square waves, where

$$\begin{aligned} v_{\text{AB}}(\theta) &= \tfrac{1}{2}S(\theta - \theta_{\text{a}}) + \tfrac{1}{2}S(\theta - \theta_{\text{c}}) \\ v_{\text{CD}}(\theta) &= \tfrac{M}{2}S(\theta - \theta_{\text{b}}) + \tfrac{M}{2}S(\theta - \theta_{\text{d}}). \end{aligned} \quad (4)$$

The inductor voltage $v_{\text{L}}(\theta)$ is the difference of $v_{\text{AB}}(\theta)$ and $v_{\text{CD}}(\theta)$. $v_{\text{L}}(\theta)$ and the inductor current $i_{\text{L}}(\theta)$ can be constructed by four standard square/ triangular waves, where

$$\begin{aligned} v_{\text{L}}(\theta) &= \frac{1}{2}S(\theta - \theta_{\text{a}}) + \frac{1}{2}S(\theta - \theta_{\text{c}}) \\ &\quad - \frac{M}{2}S(\theta - \theta_{\text{b}}) - \frac{M}{2}S(\theta - \theta_{\text{d}}) \\ i_{\text{L}}(\theta) &= \frac{1}{2}T(\theta - \theta_{\text{a}}) + \frac{1}{2}T(\theta - \theta_{\text{c}}) \\ &\quad - \frac{M}{2}T(\theta - \theta_{\text{b}}) - \frac{M}{2}T(\theta - \theta_{\text{d}}). \end{aligned} \quad (5)$$

According to (2), the average value of $v_{AB}(\theta)$, $v_{CD}(\theta)$, $v_L(\theta)$, and $i_L(\theta)$ are zero. Power transmission P and the rms values of $v_{AB}(\theta)$, $v_{CD}(\theta)$, $v_L(\theta)$, and $i_L(\theta)$ are related to the integration of the product of $S(\theta)$ and $T(\theta)$.

The integration of $S(\theta-\theta_1)$ $S(\theta-\theta_2)$, $T(\theta-\theta_1)$ $T(\theta-\theta_2)$, and $S(\theta-\theta_1)$ $T(\theta-\theta_2)$ when $\theta_1\in[-\pi, \pi]$ and $\theta_2\in[-\pi, \pi]$ are denoted as $v(\theta_1, \theta_2)$, $i(\theta_1, \theta_2)$, and $p(\theta_1, \theta_2)$, which are given as

$$v(\theta_1,\theta_2)=\int_0^{\pi} S(\theta-\theta_1)\,S(\theta-\theta_2)d\theta = \begin{cases} \pi+2(\theta_1-\theta_2), \text{Cond1}\wedge\text{Cond6} \\ \pi-2(\theta_1-\theta_2), \text{Cond2}\wedge\text{Cond5} \\ (\theta_1-\theta_2)-3\pi, \text{Cond3} \\ -(\theta_1-\theta_2)-3\pi, \text{Cond4} \end{cases} \tag{6}$$

$$i(\theta_1,\theta_2)=\int_0^{\pi} T(\theta-\theta_1)\,T(\theta-\theta_2)d\theta=\frac{1}{12} \begin{cases} \pi^3-6\pi(\theta_1-\theta_2)^2-4(\theta_1-\theta_2)^3, \text{Cond1}\wedge\text{Cond6} \\ \pi^3-6\pi(\theta_1-\theta_2)^2+4(\theta_1-\theta_2)^3, \text{Cond2}\wedge\text{Cond5} \\ 9\pi^3-6\pi^2(\theta_1-\theta_2)+6\pi(\theta_1-\theta_2)^2-4(\theta_1-\theta_2)^3, \text{Cond3} \\ 9\pi^3+6\pi^2(\theta_1-\theta_2)+6\pi(\theta_1-\theta_2)^2+4(\theta_1-\theta_2)^3, \text{Cond4} \end{cases} \tag{7}$$

$$p(\theta_1,\theta_2)=\int_0^{\pi} S(\theta-\theta_1)\,T(\theta-\theta_2)d\theta = \begin{cases} (\theta_1-\theta_2)(\pi+\theta_1-\theta_2), \text{Cond1}\wedge\text{Cond6} \\ (\theta_1-\theta_2)(\pi-\theta_1+\theta_2), \text{Cond2}\wedge\text{Cond5} \\ (\pi-\theta_1+\theta_2)(2\pi-\theta_1+\theta_2), \text{Cond3} \\ -(\pi+\theta_1-\theta_2)(2\pi+\theta_1-\theta_2), \text{Cond4}. \end{cases} \tag{8}$$

Cond1 to Cond6 show the relations of θ_1 and θ_2, where

$$\begin{cases} \text{Cond1}=\theta_2\in[-\pi,0]\wedge\theta_1\in[-\pi,\theta_2] \\ \text{Cond2}=\theta_2\in[-\pi,0]\wedge\theta_1\in[\theta_2,\theta_2+\pi] \\ \text{Cond3}=\theta_2\in[-\pi,0]\wedge\theta_1\in[\theta_2+\pi,\pi] \\ \text{Cond4}=\theta_2\in[0,\pi]\wedge\theta_1\in[-\pi,-\pi+\theta_2] \\ \text{Cond5}=\theta_2\in[0,\pi]\wedge\theta_1\in[-\pi+\theta_2,\theta_2] \\ \text{Cond6}=\theta_2\in[0,\pi]\wedge\theta_1\in[\theta_2,\theta_2+\pi]. \end{cases} \tag{9}$$

On combining (6)–(9), the DAB is divided into 12 operation regions, the region conditions and the corresponding power range are summarized in Table II. According to Table II, the control coordinate forms a spatial rectangular coordinate system, each operation region restricted by the region condition forms a triangular pyramid depicted in Fig. 3.

TABLE II
REGION CONDITIONS, AND POWER RANGE OF DIFFERENT REGIONS

Region	Region conditions	Power Range
1	$\alpha\in[0,\pi]\wedge\varphi_1\in[\alpha,\pi]\wedge\alpha+\varphi_2\in[0,\varphi_1]$	[-1/2,1/2]
2	$\alpha\in[0,\pi]\wedge\varphi_1\in[\alpha,\pi]\wedge\alpha+\varphi_2\in[\varphi_1,\pi]$	[0,2/3]
3	$\alpha\in[0,\pi]\wedge\varphi_1\in[\alpha,\pi]\wedge\alpha+\varphi_2\in[\pi,2\pi]$	[0,1]
4	$\alpha\in[0,\pi]\wedge\varphi_1\in[0,\alpha]\wedge\alpha+\varphi_2\in[0,\pi]$	[0,1/2]
5	$\alpha\in[0,\pi]\wedge\varphi_1\in[0,\alpha]\wedge\alpha+\varphi_2\in[\pi,\varphi_1+\pi]$	[0,2/3]
6	$\alpha\in[0,\pi]\wedge\varphi_1\in[0,\alpha]\wedge\alpha+\varphi_2\in[\varphi_1+\pi,2\pi]$	[-1/2,1/2]
7	$\alpha\in[-\pi,0]\wedge\varphi_1\in[\alpha+\pi,\pi]\wedge\alpha+\varphi_2\in[-\pi,-\pi+\varphi_1]$	[-1/2,1/2]
8	$\alpha\in[-\pi,0]\wedge\varphi_1\in[\alpha+\pi,\pi]\wedge\alpha+\varphi_2\in[-\pi+\varphi_1,0]$	[-2/3,0]
9	$\alpha\in[-\pi,0]\wedge\varphi_1\in[\alpha+\pi,\pi]\wedge\alpha+\varphi_2\in[0,\varphi_1]$	[-1,0]
10	$\alpha\in[-\pi,0]\wedge\varphi_1\in[0,\alpha+\pi]\wedge\alpha+\varphi_2\in[-\pi,0]$	[-1/2,0]
11	$\alpha\in[-\pi,0]\wedge\varphi_1\in[0,\alpha+\pi]\wedge\alpha+\varphi_2\in[0,\varphi_1]$	[-2/3,0]
12	$\alpha\in[-\pi,0]\wedge\varphi_1\in[0,\alpha+\pi]\wedge\alpha+\varphi_2\in[\varphi_1,\pi]$	[-1/2,1/2]

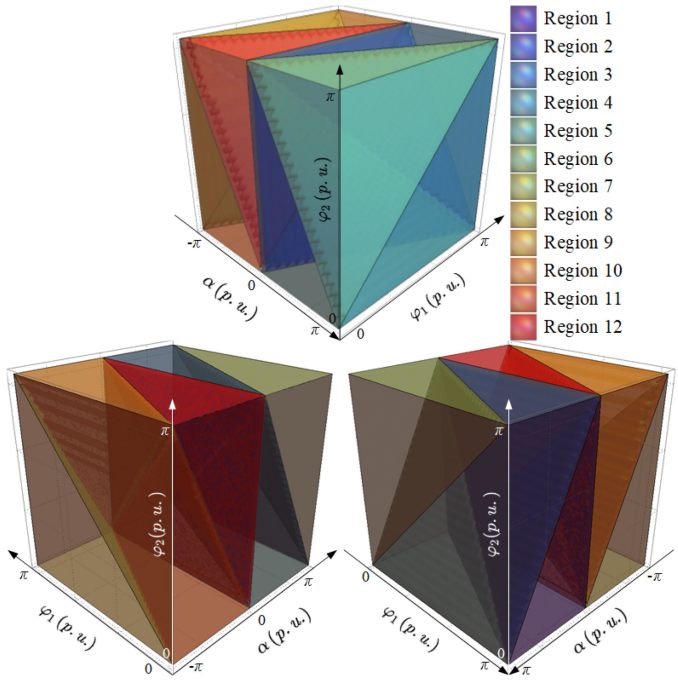

Fig. 3. In total, 12 operation regions of DAB from three different viewing angles.

$$P_{AB}=\frac{\underbrace{p(\theta_a,\theta_a)}_{0}+\underbrace{p(\theta_c,\theta_c)}_{0}+\underbrace{p(\theta_a,\theta_c)+p(\theta_c,\theta_a)}_{0}}{M\pi^2} \frac{-Mp(\theta_a,\theta_b)-Mp(\theta_a,\theta_d)-Mp(\theta_c,\theta_b)-Mp(\theta_c,\theta_d)}{M\pi^2} =\frac{p(\theta_b,\theta_a)+p(\theta_b,\theta_c)-p(\theta_c,\theta_d)-p(\theta_a,\theta_d)}{\pi^2}$$

$$P_{CD}=\frac{Mp(\theta_b,\theta_a)+Mp(\theta_b,\theta_c)+Mp(\theta_d,\theta_a)+Mp(\theta_d,\theta_c) \underbrace{-M^2p(\theta_b,\theta_b)}_{0}\underbrace{-M^2p(\theta_d,\theta_d)}_{0}\underbrace{-M^2p(\theta_b,\theta_d)-M^2p(\theta_d,\theta_b)}_{0}}{M\pi^2} =\frac{p(\theta_b,\theta_a)+p(\theta_b,\theta_c)-p(\theta_c,\theta_d)-p(\theta_a,\theta_d)}{\pi^2} \tag{13}$$

Instantaneous input and output power are denoted as $p_{\mathrm{AB}}(\theta)$ and $p_{\mathrm{CD}}(\theta)$, which are given as

$$p_{\mathrm{AB}}(\theta) = v_{\mathrm{AB}}(\theta)\, i_{\mathrm{L}}(\theta)\,; p_{\mathrm{CD}}(\theta) = v_{\mathrm{CD}}(\theta)\, i_{\mathrm{L}}(\theta)\,. \quad (10)$$

The normalized average power of $p_{\mathrm{AB}}(\theta)$ and $p_{\mathrm{CD}}(\theta)$ are denoted as P_{AB} and P_{CD}, which are given as

$$P_{\mathrm{AB}} = \frac{4}{M\pi^2}\int_0^{\pi} p_{\mathrm{AB}}(\theta)\, d\theta, P_{\mathrm{CD}} = \frac{4}{M\pi^2}\int_0^{\pi} p_{\mathrm{CD}}(\theta)\, d\theta. \quad (11)$$

From (8), $p(\theta_1, \theta_2)$ is anticommutative, where

$$p(\theta_1, \theta_2) + p(\theta_2, \theta_1) = 0 \quad (12)$$

Assume there is no power loss, the power balance equation is given as $P = P_{\mathrm{AB}} = P_{\mathrm{CD}}$, where, eq. (13) shown at the bottom of the previous page.

The expressions of P are given in the Appendix.

From (6)–(7), $v(\theta_1, \theta_2)$ and $i(\theta_1, \theta_2)$ are commutative, where

$$v(\theta_1, \theta_2) = v(\theta_2, \theta_1)\,; i(\theta_1, \theta_2) = i(\theta_2, \theta_1)\,. \quad (14)$$

The rms value of $v_{\mathrm{AB}}(\theta)$ and $v_{\mathrm{CD}}(\theta)$ are denoted as $v_{\mathrm{AB\text{-}rms}}$ and $v_{\mathrm{CD\text{-}rms}}$ and are with simple expressions where

$$v_{\mathrm{AB-rms}} = \sqrt{\frac{\varphi_1}{\pi}}; v_{\mathrm{CD-rms}} = \sqrt{\frac{M^2\varphi_2}{\pi}}. \quad (15)$$

The rms value of $i_{\mathrm{L}}(\theta)$ and $v_{\mathrm{L}}(\theta)$ are denoted as I_{rms} and V_{rms}, which can be calculated by

$$I_{\mathrm{rms}} = \sqrt{\frac{\begin{array}{l} i(\theta_{\mathrm{a}}, \theta_{\mathrm{a}}) - 2Mi(\theta_{\mathrm{a}}, \theta_{\mathrm{b}}) + 2i(\theta_{\mathrm{a}}, \theta_{\mathrm{c}}) - 2Mi(\theta_{\mathrm{a}}, \theta_{\mathrm{d}}) \\ + M^2 i(\theta_{\mathrm{b}}, \theta_{\mathrm{b}}) - 2Mi(\theta_{\mathrm{b}}, \theta_{\mathrm{c}}) - 2M^2 i(\theta_{\mathrm{b}}, \theta_{\mathrm{d}}) \\ + i(\theta_{\mathrm{c}}, \theta_{\mathrm{c}}) - 2Mi(\theta_{\mathrm{c}}, \theta_{\mathrm{d}}) \\ + M^2 i(\theta_{\mathrm{d}}, \theta_{\mathrm{d}}) \end{array}}{4\pi}}$$

$$V_{\mathrm{rms}} = \sqrt{\frac{\begin{array}{l} v(\theta_{\mathrm{a}}, \theta_{\mathrm{a}}) - 2Mv(\theta_{\mathrm{a}}, \theta_{\mathrm{b}}) + 2v(\theta_{\mathrm{a}}, \theta_{\mathrm{c}}) - 2Mv(\theta_{\mathrm{a}}, \theta_{\mathrm{d}}) \\ + M^2 v(\theta_{\mathrm{b}}, \theta_{\mathrm{b}}) - 2Mv(\theta_{\mathrm{b}}, \theta_{\mathrm{c}}) - 2M^2 v(\theta_{\mathrm{b}}, \theta_{\mathrm{d}}) \\ + v(\theta_{\mathrm{c}}, \theta_{\mathrm{c}}) - 2Mv(\theta_{\mathrm{c}}, \theta_{\mathrm{d}}) \\ + M^2 v(\theta_{\mathrm{d}}, \theta_{\mathrm{d}}) \end{array}}{4\pi}}. \quad (16)$$

The expressions of I_{rms} and V_{rms} are different in 12 regions and are summarized in the Appendix. Apparent power can be calculated with $S_{\mathrm{AB}} = v_{\mathrm{AB\text{-}rms}}\, I_{\mathrm{rms}}$, $S_{\mathrm{CD}} = v_{\mathrm{CD\text{-}rms}}\, I_{\mathrm{rms}}$.

I_{Peak} appears at the changing point of $i_{\mathrm{L}}(\theta)$ and is given as

$$I_{\mathrm{Peak}} = \max\left(|i_{\mathrm{L}}(\theta_{\mathrm{a}})|, |i_{\mathrm{L}}(\theta_{\mathrm{b}})|, |i_{\mathrm{L}}(\theta_{\mathrm{c}})|, |i_{\mathrm{L}}(\theta_{\mathrm{d}})|\right). \quad (17)$$

The ZVS conditions are also related to $i_{\mathrm{L}}(\theta_{\mathrm{a}})$, $i_{\mathrm{L}}(\theta_{\mathrm{b}})$, $i_{\mathrm{L}}(\theta_{\mathrm{c}})$, and $i_{\mathrm{L}}(\theta_{\mathrm{d}})$, which are summarized in Table III, where

$$i_{\mathrm{L1}} = -\frac{\varphi_1 - M\varphi_2}{2}; i_{\mathrm{L2}} = M(\pi - \alpha) - \frac{\varphi_1 + M\varphi_2}{2}$$

$$i_{\mathrm{L3}} = \alpha - \frac{\varphi_1 - M\varphi_2}{2}; i_{\mathrm{L4}} = \pi + \alpha - \frac{\varphi_1 + M\varphi_2}{2}$$

TABLE III
ZVS CONDITIONS IN DIFFERENT REGIONS

Region	ZVS conditions
1	$i_{\mathrm{L1}} \le 0 \wedge i_{\mathrm{L3}} \ge 0 \wedge i_{\mathrm{L7}} \le 0$
2	$i_{\mathrm{L1}} = 0 \wedge i_{\mathrm{L3}} \ge 0 \wedge i_{\mathrm{L9}} \ge 0$
3	$i_{\mathrm{L2}} \le 0 \wedge i_{\mathrm{L3}} \ge 0 \wedge i_{\mathrm{L9}} \ge 0 \wedge i_{\mathrm{L11}} \ge 0$
4	$i_{\mathrm{L1}} \le 0 \wedge i_{\mathrm{L6}} \ge 0$
5	$i_{\mathrm{L1}} \le 0 \wedge i_{\mathrm{L2}} \le 0 \wedge i_{\mathrm{L6}} \ge 0$
6	$i_{\mathrm{L2}} \le 0 \wedge i_{\mathrm{L6}} \ge 0 \wedge i_{\mathrm{L11}} \ge 0$
7	$i_{\mathrm{L6}} \ge 0 \wedge i_{\mathrm{L8}} \le 0 \wedge i_{\mathrm{L11}} \ge 0$
8	$i_{\mathrm{L6}} \ge 0 \wedge i_{\mathrm{L8}} \le 0 \wedge i_{\mathrm{L10}} \ge 0$
9	$i_{\mathrm{L5}} \le 0 \wedge i_{\mathrm{L7}} \ge 0 \wedge i_{\mathrm{L8}} \ge 0 \wedge i_{\mathrm{L10}} \ge 0$
10	$i_{\mathrm{L1}} \le 0 \wedge i_{\mathrm{L5}} \ge 0$
11	$i_{\mathrm{L1}} = 0 \wedge i_{\mathrm{L5}} \le 0 \wedge i_{\mathrm{L7}} \ge 0$
12	$i_{\mathrm{L1}} \le 0 \wedge i_{\mathrm{L5}} \le 0 \wedge i_{\mathrm{L8}} \ge 0$

$$i_{\mathrm{L5}} = M\alpha - \frac{\varphi_1 - M\varphi_2}{2}; i_{\mathrm{L6}} = \frac{\varphi_1 + M\varphi_2}{2}$$

$$i_{\mathrm{L7}} = \alpha + \varphi_2 - \frac{\varphi_1 - M\varphi_2}{2}; i_{\mathrm{L8}} = \pi + \alpha - \frac{\varphi_1 + M\varphi_2}{2}$$

$$i_{\mathrm{L9}} = \frac{\varphi_1 + M(2\alpha - 2\varphi_1 + \varphi_2)}{2};$$

$$i_{\mathrm{L10}} = \frac{\varphi_1 + \varphi_2}{2} - M(\pi + \alpha - \varphi_1)$$

$$i_{\mathrm{L11}} = \alpha + \varphi_2 - \pi - \frac{\varphi_1 - M\varphi_2}{2}. \quad (18)$$

Due to the symmetric characteristic of DAB, region x and region $x + 6$ ($x = 1, \ldots 6$) are with similar expressions of electric quantities and ZVS conditions.

B. Frequency Domain Analysis

The frequency domain analysis of DAB starts with the Fourier expansion of $S(\theta)$ and $T(\theta)$, where

$$S(\theta) = \frac{4}{\pi}\sum_{\mathrm{i}=1}^{\infty}\frac{\sin((2i-1)\theta)}{2i-1},$$

$$T(\theta) = -\frac{4}{\pi}\sum_{\mathrm{i}=1}^{\infty}\frac{\cos((2i-1)\theta)}{(2i-1)^2}. \quad (19)$$

The nth Fourier sine and cosine coefficients of $v_{\mathrm{AB}}(\theta)$, $v_{\mathrm{CD}}(\theta)$, and $i_{\mathrm{L}}(\theta)$ are denoted as $v_{\mathrm{ABs}}(n)$, $v_{\mathrm{ABc}}(n)$, $v_{\mathrm{CDs}}(n)$, $v_{\mathrm{CDc}}(n)$, $i_{\mathrm{Ls}}(n)$, and $i_{\mathrm{Lc}}(n)$, which can be obtained as

$$v_{\mathrm{ABs}}(n) = \frac{2}{n\pi}(1 - \cos(n\varphi_1))$$

$$v_{\mathrm{ABc}}(n) = \frac{2}{n\pi}\sin(n\varphi_1)$$

$$v_{\mathrm{CDs}}(n) = \frac{2M}{n\pi}(\cos(n\alpha) + \cos(n\alpha + n\varphi_2))$$

$$v_{\mathrm{CDc}}(n) = -\frac{2M}{n\pi}(\sin(n\alpha) + \sin(n\alpha + n\varphi_2))$$

$$i_{\mathrm{Ls}}(n) = \frac{2}{n^2\pi}(\sin(n\varphi_1) + M(\sin(n\alpha) - \sin(n\alpha + n\varphi_2)))$$

$$i_{\mathrm{Lc}}(n)=\frac{2}{n^2\pi}\left(\cos(n\varphi_1)-1+M\left(\cos(n\alpha)-\cos(n\alpha+n\varphi_2)\right)\right). \tag{20}$$

The nth sine and cosine coefficients of $p_{\mathrm{AB}}(\theta)$ and $p_{\mathrm{CD}}(\theta)$ are denoted as $p_{\mathrm{ABs}}(n)$, $p_{\mathrm{ABc}}(n)$, $p_{\mathrm{CDs}}(n)$, and $p_{\mathrm{CDc}}(n)$, which can be derived from $v_{\mathrm{AB}}(\theta)$, $v_{\mathrm{CD}}(\theta)$, and $i_{\mathrm{L}}(\theta)$ from discrete convolution and correlation in

$$\begin{cases} p_{\mathrm{ABs}}(n)=v_{\mathrm{ABs}}(n)\otimes i_{\mathrm{Lc}}(n)-v_{\mathrm{ABc}}(n)\otimes i_{\mathrm{Ls}}(n) \\ \quad +v_{\mathrm{ABs}}(n)*i_{\mathrm{Lc}}(n)-v_{\mathrm{ABc}}(n)*i_{\mathrm{Ls}}(n) \\ p_{\mathrm{ABc}}(n)=v_{\mathrm{ABc}}(n)\otimes i_{\mathrm{Lc}}(n)+v_{\mathrm{ABs}}(n)\otimes i_{\mathrm{Ls}}(n) \\ \quad +v_{\mathrm{ABc}}(n)*i_{\mathrm{Lc}}(n)-v_{\mathrm{ABs}}(n)*i_{\mathrm{Ls}}(n) \\ p_{\mathrm{CDs}}(n)=v_{\mathrm{CDs}}(n)\otimes i_{\mathrm{Lc}}(n)-v_{\mathrm{CDc}}(n)\otimes i_{\mathrm{Ls}}(n) \\ \quad +v_{\mathrm{CDs}}(n)*i_{\mathrm{Lc}}(n)-v_{\mathrm{CDc}}(n)*i_{\mathrm{Ls}}(n) \\ p_{\mathrm{CDc}}(n)=v_{\mathrm{CDc}}(n)\otimes i_{\mathrm{Lc}}(n)+v_{\mathrm{CDs}}(n)\otimes i_{\mathrm{Ls}}(n) \\ \quad +v_{\mathrm{CDc}}(n)*i_{\mathrm{Lc}}(n)-v_{\mathrm{CDs}}(n)*i_{\mathrm{Ls}}(n) \end{cases} \tag{21}$$

where $\otimes$ and $*$ denote discrete convolution and correlation

$$\begin{aligned} v_{\mathrm{ABs}}(n)*i_{\mathrm{Lc}}(n)&=\sum_{x=-\infty}^{\infty}v_{\mathrm{ABs}}(x)\,i_{\mathrm{Lc}}(n-x) \\ v_{\mathrm{ABs}}(n)\otimes i_{\mathrm{Lc}}(n)&=\sum_{x=-\infty}^{\infty}v_{\mathrm{ABs}}(x)\,i_{\mathrm{Lc}}(x-n). \end{aligned} \tag{22}$$

Based on the standard waveform function $S(\theta)$ and $T(\theta)$, the unified description model of DAB, including all the time and frequency domain electric quantities, can be derived.

III. Unified Optimization Method of DAB

A unified optimization method of DAB is introduced in this section with three steps. In Section III-A: Feasible region analysis. In Section III-B: Tangent point searching. In Section III-C: Control coordinate calculation and operation region division.

First, the unified optimization problem of DAB can be mathematically presented as

$$\begin{aligned} &\mathrm{Min}\,(A(\mathbf{X})) \\ &\mathrm{Subject\ to} \\ &P(\mathbf{X})-P=0\wedge B_{\mathrm{i}}(\mathbf{X})\le 0, i=1,\cdots q \end{aligned} \tag{23}$$

where $\mathbf{X}=(\alpha,\varphi_1,\varphi_2)$, is the control coordinate, $A(\mathbf{X})$ is the optimization objective, $P(\mathbf{X})$ is the equality constraint condition by P, and $B_{\mathrm{i}}(\mathbf{X})\le 0$, $i=1,\ldots q$ are feasible region restraints in Table II. If ZVS conditions are taken into consideration, inequalities in Table III should also be added to $B_{\mathrm{i}}(\mathbf{X})$.

A. Feasible Region Analysis

With the abovementioned analysis in Section II, the operation of DAB is divided into 12 regions with overlapping power ranges. Six examples of the control coordinate trajectories (CCTs) with $P=-0.8$, $P=-0.6$, $P=-0.4$, $P=0.4$, $P=0.6$, and $P=0.8$ are depicted in Fig. 4. In Fig. 4, the CCTs with different P form different three-dimensional (3-D) surfaces and the boundary lines are colored in red. According to the power range of different regions, the CCTs are divided into different regions. When $P\in[-1,\ -2/3]$, the CCTs only located in region 9 in Fig. 4(a). When $P\in[-2/3,\ -1/2]$, the CCTs are divided into 3 parts with regions 8, 9, and 11 in Fig. 4(b). When $P\in[-1/2, 0]$, the CCTs are divided into 8 parts with regions 1, 6, 7, 8, 9, 10, 11, and 12 in Fig. 4(c). Similarly, when $P\in[0,\ 1/2]$, the CCTs are divided into 8 parts with regions 1, 2, 3, 4, 5, 6, 7, and 12 in Fig. 4(d). When $P\in[1/2,\ 2/3]$, the CCTs are divided into 3 parts with regions 2, 3, and 5 in Fig. 4(e). When $P\in[2/3,\ 1]$, the CCTs only located in region 3 in Fig. 4(f).

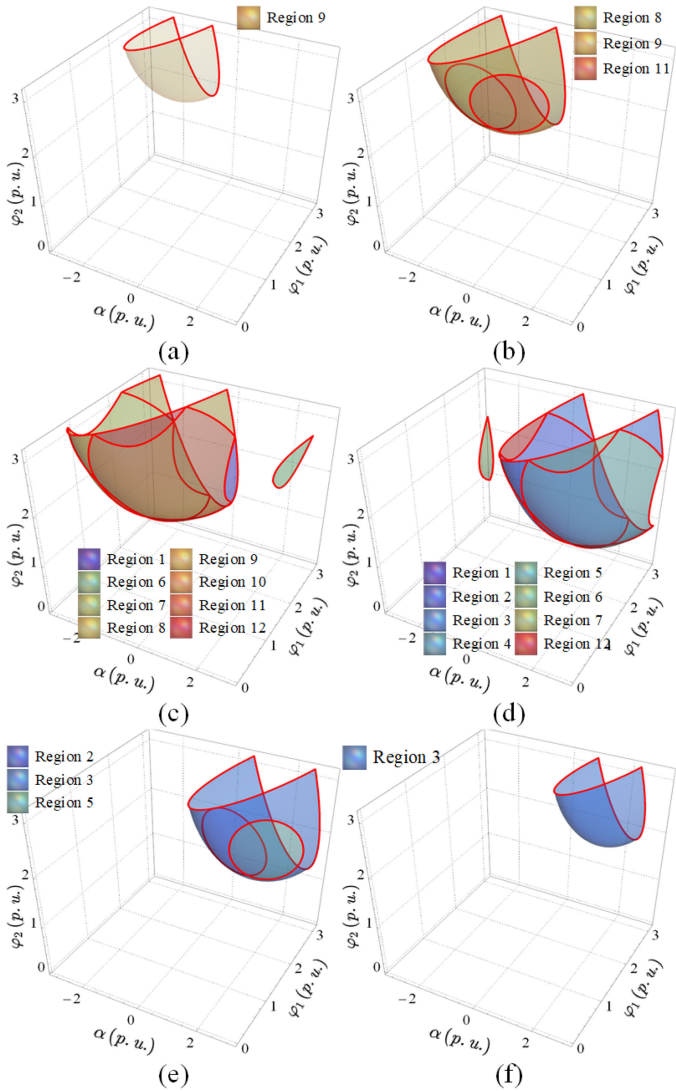

Fig. 4. CCTs of DAB with different power transmission P. (a) $P=-0.8$. (b) $P=-0.6$. (c) $P=-0.4$. (d) $P=0.4$. (e) $P=0.6$. (f) $P=0.8$.

With $|P|$ decreasing, the CCTs are divided into more regions. Although the continuous property preserves for the regions 1, 4, 6, 7, 10, and 12, two hollows appear in regions 3, and 9 when $|P|\in[1/2,\ 2/3]$. When $|P|\in[0,\ 1/2]$, regions 2, 5, 8, and 11 are nonconvex, and regions 3, and 9 are with four discontinuous pieces. Since the feasible region restricted by P is not a convex set, regular convex optimization methods are ineffective, and novel methods are required to solve this optimization problem.

B. Tangent Point Searching

When P is given, the control coordinate is fixed in a specified CCT, which forms a 3-D surface of feasible region. The next process is to draw the 3-D contour map of the objective function.

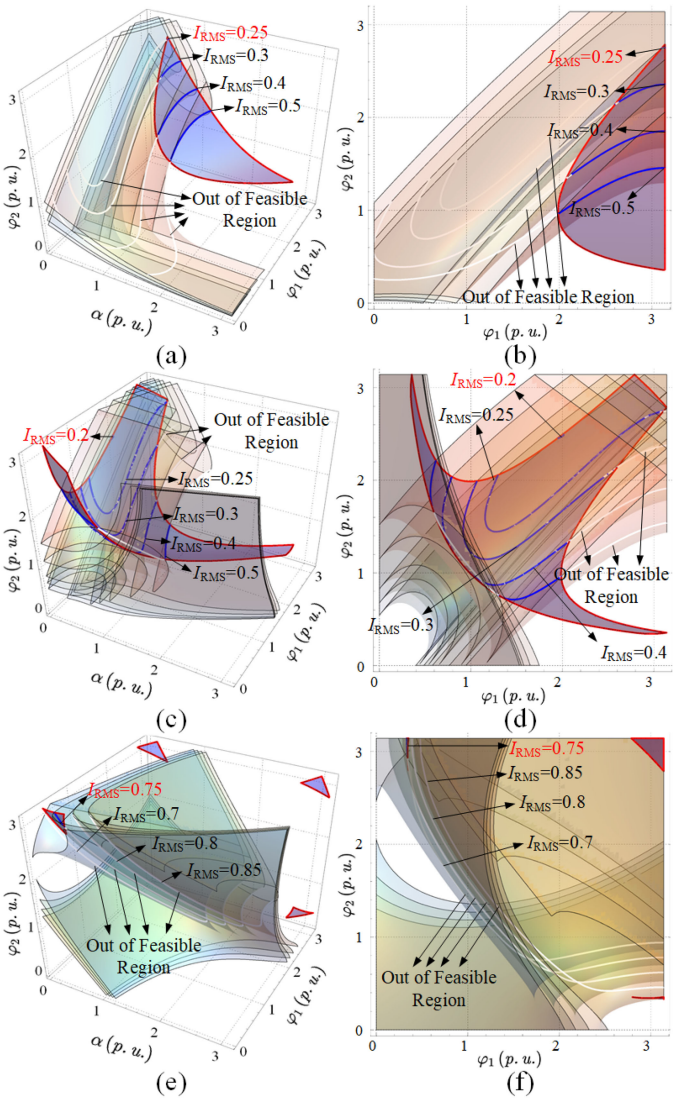

Fig. 5. Three-dimensional contour maps of $I_{\rm rms}$. (a) In region 1. (b) Right view map in region 1. (c) In region 2. (d) Right view map in region 2. (e) In region 3. (f) Right view map in region 3.

Take $I_{\rm rms}$ as an example, when $M = 0.8$, $P = 0.2$, the 3-D contour maps of multiple values of $I_{\rm rms}$ are depicted in Fig. 5, where the red surface is the feasible region with $P = 0.2$ and multiple surfaces colored in light orange, yellow, green, and blue are with different $I_{\rm rms}$. The intersections when the region condition is discarded/considered are colored in white/red, respectively.

With continuously decreasing $I_{\rm rms}$, the intersections tend to shrink and finally shrink into the tangent point, which indicates that the local minimum $I_{\rm rms}$ is found. The local minimum of $I_{\rm rms}$ in region 1 is 0.25 while it is 0.2 in region 2, and 0.75 in region 3.

Since the two surfaces are tangent at the tangent point, the normal vectors of the two surfaces are parallel at the tangent point. Note that this condition is established only when the tangent point is located in the feasible region. Otherwise, the tangent point is unavailable, and the local minimum is reached at the boundary of the feasible region.

Denote the local minimum of $A(\mathbf{X})$ as A irrelevant to $\mathbf{X}$, the surfaces of $P(\mathbf{X})$ and $A(\mathbf{X})$ are given as

$$P(\mathbf{X}) - P = 0; A(\mathbf{X}) - A = 0. \tag{24}$$

The normal vectors of the two surfaces $P(\mathbf{X})$ and $A(\mathbf{X})$ are denoted as $\boldsymbol{n}_{\mathbf{P}}$ and $\boldsymbol{n}_{\mathbf{A}}$, where

$$\begin{aligned} \boldsymbol{n}_{\mathbf{P}} &= \left[\frac{\partial P(\mathbf{X})}{\partial \alpha} \frac{\partial P(\mathbf{X})}{\partial \varphi_1} \frac{\partial P(\mathbf{X})}{\partial \varphi_2}\right] \\ \boldsymbol{n}_{\mathbf{A}} &= \left[\frac{\partial A(\mathbf{X})}{\partial \alpha} \frac{\partial A(\mathbf{X})}{\partial \varphi_1} \frac{\partial A(\mathbf{X})}{\partial \varphi_2}\right]. \end{aligned} \tag{25}$$

Denote $\mathbf{X}_{\rm opt}$ as the control coordinate with minimum $A(\mathbf{X})$ when $P(\mathbf{X})$ is given. If $\mathbf{X}_{\rm opt}$ is located in the operation region, $\mathbf{X}_{\rm opt}$ is the tangent point of the two surfaces, $\boldsymbol{n}_{\mathbf{P}}$ and $\boldsymbol{n}_{\mathbf{A}}$ should be parallel, where

$$\boldsymbol{n}_{\mathbf{P}} // \boldsymbol{n}_{\mathbf{A}} \Rightarrow \begin{cases} \dfrac{\partial A(\mathbf{X}_{\rm opt})}{\partial \alpha} \Big/ \dfrac{\partial P(\mathbf{X}_{\rm opt})}{\partial \alpha} = \dfrac{\partial A(\mathbf{X}_{\rm opt})}{\partial \varphi_1} \Big/ \dfrac{\partial P(\mathbf{X}_{\rm opt})}{\partial \varphi_1} \\ \dfrac{\partial A(\mathbf{X}_{\rm opt})}{\partial \varphi_1} \Big/ \dfrac{\partial P(\mathbf{X}_{\rm opt})}{\partial \varphi_1} = \dfrac{\partial A(\mathbf{X}_{\rm opt})}{\partial \varphi_2} \Big/ \dfrac{\partial P(\mathbf{X}_{\rm opt})}{\partial \varphi_2}. \end{cases} \tag{26}$$

Besides, the surface of $A(\mathbf{X})$ at $\mathbf{X}_{\rm opt}$ should be convex to guarantee the minimum value. The convexity of $A(\mathbf{X})$ at $\mathbf{X}_{\rm opt}$ is estimated by the Hessian matrix denoted as $H_{\rm A}(\mathbf{X})$, where

$$H_{\rm A}(\mathbf{X}) = \begin{bmatrix} \dfrac{\partial^2 A(\mathbf{X})}{\partial \alpha^2} & \dfrac{\partial^2 A(\mathbf{X})}{\partial \alpha \partial \varphi_1} & \dfrac{\partial^2 A(\mathbf{X})}{\partial \alpha \partial \varphi_2} \\ \dfrac{\partial^2 A(\mathbf{X})}{\partial \varphi_1 \partial \alpha} & \dfrac{\partial^2 A(\mathbf{X})}{\partial {\varphi_1}^2} & \dfrac{\partial^2 A(\mathbf{X})}{\partial \varphi_1 \partial \varphi_2} \\ \dfrac{\partial^2 A(\mathbf{X})}{\partial \varphi_2 \partial \alpha} & \dfrac{\partial^2 A(\mathbf{X})}{\partial \varphi_2 \partial \varphi_1} & \dfrac{\partial^2 A(\mathbf{X})}{\partial {\varphi_2}^2} \end{bmatrix}. \tag{27}$$

Because $A(\mathbf{X})$ is second order differential, $H_{\rm A}(\mathbf{X})$ is a symmetric matrix. If the surface of $A(\mathbf{X})$ is convex at $\mathbf{X}_{\rm opt}$, $H_{\rm A}(\mathbf{X}_{\rm opt})$ should be positive semidefinite, and the eigenvalues of $H_{\rm A}(\mathbf{X}_{\rm opt})$ are non-negative. If $\mathbf{X}_{\rm opt}$ is located out of the operation region, $H_{\rm A}(\mathbf{X}_{\rm opt})$ does not have to be positive semidefinite.

C. Control Coordinate Calculation and Operation Region Division

Apply the tangent point searching method to all regions, and select the minimum of all the local minimums, the control coordinate, and operation region with $P \in [-1, 1]$, $M \in (0, \infty)$ can be obtained. Because there are 12 regions of DAB, it will be time-consuming if the optimization method has to be repeated 12 times. There are some tips in the optimization of DAB.

If one $\mathbf{X}_{\rm opt}$ when $P \in [0, 1]$, $M \in (0, 1)$ is obtained, the dual $\mathbf{X}_{\rm opt}$ with $P \in [-1, 0]$, $M \in (1, \infty)$ or with $P \in [0, 1]$, $M \in (1, \infty)$ can also be obtained by proper manipulating $(\alpha, \varphi_1, \varphi_2)$. Hence, only $P \in [0, 1]$ needs to be considered. From the operation region point of view, only regions 1–6 need to be considered due to the symmetric expressions of electric quantities in regions 7–12. In regions 4–6, the instantaneous power has to be stored in L before being transmitted, which leads to a larger $i_{\rm L}(\theta)$ but does not result in a higher power range compared with regions 1–3. Thus, the optimization method only needs to be applied in regions 1–3.

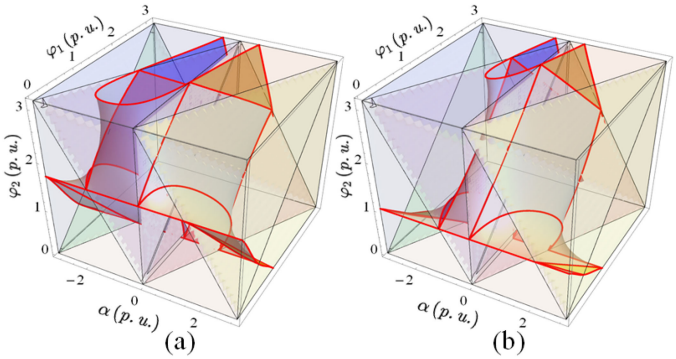

Fig. 6. Three-dimensional contour maps with $I_{\rm rms} = 0.5$. (a) $M = 0.8$. (b) $M = 1.2$.

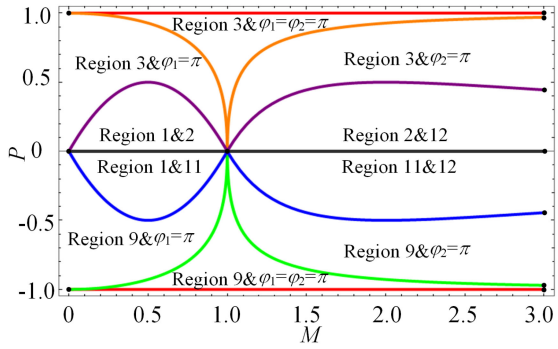

Fig. 7. Operation region with minimum $I_{\rm RMS}$.

IV. Optimization Process of DAB and the Optimization Objective Design Method

Because the loss of a DAB is closely related to $I_{\rm rms}$ and $I_{\rm Peak}$. These two optimization objectives are chosen in this section to illustrate to show how the unified optimization method works.

A. Choose I_{rms} as the Optimization Objective

The 3-D contour maps of $I_{\rm rms}$ when $M < 1$ and $M > 1$ are depicted in Fig. 6. The optimization process is as follows.

1) Optimization in Region 1: Apply (26) to region 1 and it yields

$$\alpha = 0, \varphi_1 = M\varphi_2. \tag{28}$$

The minimum is reached at the boundary of regions 1, and 2 (Region 1 and 2). The control coordinate is given as

$$\begin{aligned} &\alpha = 0, \varphi_1 = \sqrt{\tfrac{MP}{2(1-M)}}\pi, \varphi_2 = \sqrt{\tfrac{P}{2M(1-M)}}\pi \\ &\forall P \in [0, 2M\,(1-M)) \wedge M \in (0,1). \end{aligned} \tag{29}$$

2) Optimization in Region 2: Apply (26) to region 2 and it yields

$$\alpha = \varphi_1 - \varphi_2, \varphi_1 = M\varphi_2. \tag{30}$$

The minimum is reached at the boundary of region 2, and 12 (Region 2 and 12). The control coordinate is given as

$$\begin{aligned} &\alpha = \sqrt{\tfrac{P(M-1)}{2}}\pi, \varphi_1 = \sqrt{\tfrac{M^2P}{2(M-1)}}\pi, \varphi_2 = \sqrt{\tfrac{P}{2(M-1)}}\pi \\ &\forall P \in \left[0, \tfrac{2(M-1)}{M^2}\right) \wedge M \in [1,\infty)\,. \end{aligned} \tag{31}$$

3) Optimization in Region 3: Apply (26) to region 3 and the control coordinate is with

$$\begin{cases} \alpha = \frac{(M-1)\varphi_1 + \sqrt{\varphi_1(\varphi_1 + M^2(\varphi_1 - 2\pi))}}{2M}, \varphi_2 = \pi \\ \forall P \in \left[2M\,(1-M)\,, \frac{2\sqrt{1-M^2}\left(1-\sqrt{1-M^2}\right)}{M^2}\right) \wedge M \in (0,1) \\ \alpha = \frac{2\pi - (M+1)\varphi_2 + \sqrt{\varphi_2((M^2+1)\varphi_2 - 2\pi)}}{2}, \varphi_1 = \pi \\ \forall P \in \left[\frac{2(M-1)}{M^2}, 2\left(1 + M\sqrt{M^2-1} - M^2\right)\right) \wedge M \in [1,\infty)\,. \end{cases} \tag{32}$$

In (32), the control coordinate is with a quartic equation, and the analytical expressions are presented in [27]. Because there is $\varphi_1 = \pi$ or $\varphi_2 = \pi$, the minimum is reached at the boundary of region 3 and the spatial rectangular coordinate system (Region 3 and $\varphi_1 = \pi$ when $M < 1$ or Region 3 and $\varphi_2 = \pi$ when $M > 1$). When P is beyond the limit in (32), the minimum is reached at Region 3 and $\varphi_1 = \varphi_2 = \pi$ (also SPS), and the control coordinate is given as

$$\begin{cases} \alpha = \frac{\left(1-\sqrt{1-P}\right)\pi}{2}, \varphi_1 = \pi, \varphi_2 = \pi \\ \forall P \in \left[\frac{2\sqrt{1-M^2}\left(1-\sqrt{1-M^2}\right)}{M^2}, 1\right] \wedge M \in (0,1) \\ \alpha = \frac{\left(1-\sqrt{1-P}\right)\pi}{2}, \varphi_1 = \pi, \varphi_2 = \pi \\ \forall P \in \left[2\left(1 + M\sqrt{M^2-1} - M^2\right), 1\right] \wedge M \in [1,\infty)\,. \end{cases} \tag{33}$$

The abovementioned minimums are all reached at the boundary of regions 1–3. Hence, $H_{\rm A}(\mathbf{X}_{\rm opt})$ in (26) and (28)–(30) does not have to be positive semidefinite. Proper manipulate the control coordinate, and the operation region with minimum $I_{\rm rms}$ is depicted in Fig. 7.

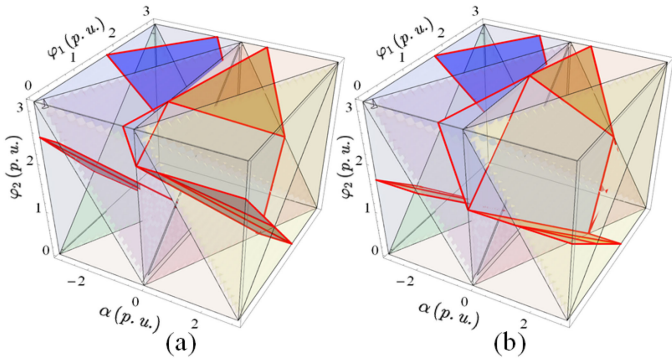

Fig. 8. Three-dimensional contour maps with $I_{\rm Peak} = 1$. (a) $M = 0.8$. (b) $M = 1.2$. .

B. Choose I_{Peak} as the Optimization Objective

$I_{\rm Peak}$ is the peak value of $i_{\rm L}$ related to the current stress of the switches. According to (17), $I_{\rm Peak}$ is an affine function of $\mathbf{X}$, and there is always $H_{\rm A}(\mathbf{X}_{\rm opt}) \equiv 0$. The 3-D contour maps of $I_{\rm Peak}$ when $M < 1$ and $M > 1$ are depicted in Fig. 8.

1) Optimization in Region 1: Apply (26) to region 1 and it is found that the tangent point does not exist.

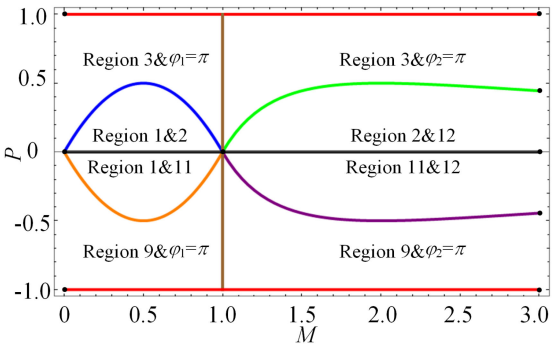

Fig. 9. Operation region with minimum I_{Peak}.

2) Optimization in Region 2: Apply (26) to region 2 and the result is the same as (28) and (29). Because the minimum is reached at the boundary of region 1, and 2 in (28), the local minimum searching in region 1 is also done in this process.

3) Optimization in Region 3: Apply (26) to region 3 and it yields

$$\begin{aligned}&\alpha=\frac{1}{2}\left(1-\sqrt{\frac{1-P}{2M^2-2M+1}}\right)\pi\\&\varphi_1=\left(1-(1-M)\sqrt{\frac{1-P}{2M^2-2M+1}}\right)\pi,\varphi_2=\pi\\&\forall P\in\left[2M\left(1-M\right),1\right]\wedge M\in(0,1)\end{aligned}\tag{34}$$

$$\begin{aligned}&\alpha=\frac{1}{2}\left(1+(M-2)\sqrt{\frac{1-P}{M^2-2M+2}}\right)\pi,\varphi_1=\pi\\&\varphi_2=\left(1-(1-M)\sqrt{\frac{1-P}{M^2-2M+2}}\right)\pi\\&\forall P\in\left[\frac{2(M-1)}{M^2},1\right]\wedge M\in[1,\infty).\end{aligned}\tag{35}$$

The operation region with minimum I_{Peak} is depicted in Fig. 9. From Figs. 7 and 9, the operation regions with minimum I_{rms}, and I_{Peak} are both symmetric with $P>0$ and $P<0$. If the abscissas are in logarithmic scale, the operation regions will be centrosymmetric with (1, 0).

C. Other Types of Optimization Objective

Because I_{Peak} is an affine function of $\mathbf{X}$, the solution of $\mathbf{X}_{\mathrm{opt}}$ is with solving a quadratic equation of M and P. I_{rms} is a cubic function of $\mathbf{X}$, the solution of $\mathbf{X}_{\mathrm{opt}}$ is with solving a quartic equation of M and P. Hence, analytical expressions of $\mathbf{X}_{\mathrm{opt}}$ can be obtained. Apart from I_{rms} and I_{Peak}, there are high order optimization objectives like S_{AB}, S_{CD}, and S_{AB}, S_{CD} from the perspective of apparent power. The optimization objective can also choose nonpolynomials of $\mathbf{X}$, and the most representative one is reactive power from port AB $|Q_{\mathrm{AB}}|$ and reactive power from port CD $|Q_{\mathrm{CD}}|$, where

$$\begin{aligned}|Q_{\mathrm{AB}}|&=\frac{16\sin(\varphi_1)}{\pi^2}\left|\sin\left(\varphi_1\right)-M\cos\left(\alpha\right)\sin\left(\varphi_2\right)\right|\\|Q_{\mathrm{CD}}|&=\frac{16M\sin(\varphi_2)}{\pi^2}\left|\cos\left(\alpha\right)\sin\left(\varphi_1\right)-M\sin\left(\varphi_2\right)\right|.\end{aligned}\tag{36}$$

When S_{AB}, S_{CD}, S_{AB} S_{CD}, $|Q_{\mathrm{AB}}|$, and $|Q_{\mathrm{CD}}|$ are chosen as the optimization objective, analytical expressions of $\mathbf{X}_{\mathrm{opt}}$ are unavailable.

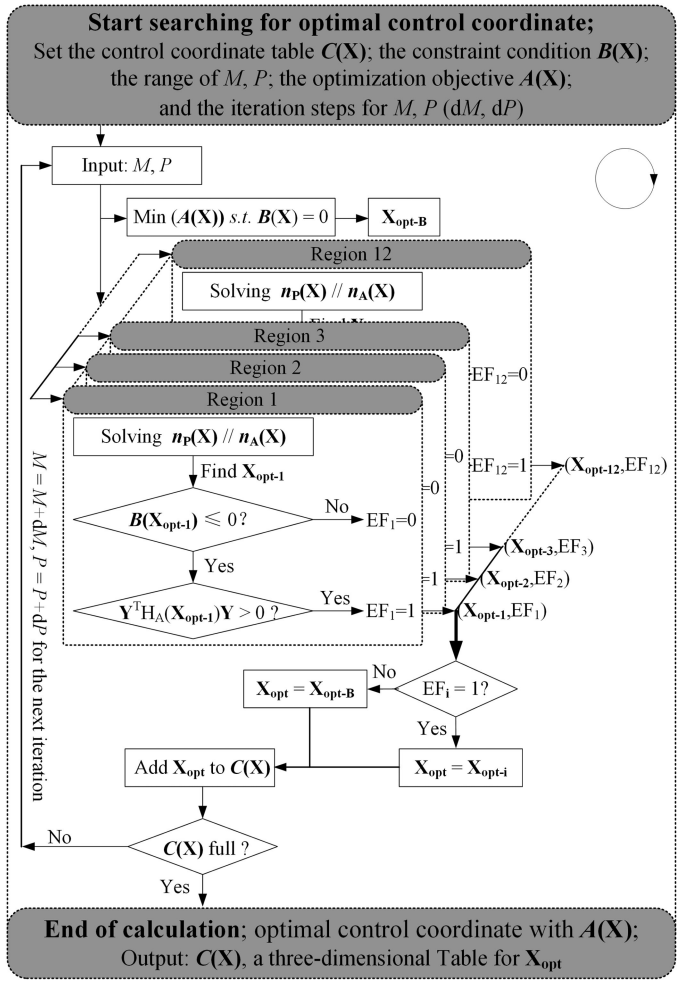

Fig. 10. Procedure to determine the optimal control coordinate with an arbitrary continuous optimization objective.

D. Universal Numerical Solution for the Optimization of DAB

Since some of the optimization objective are without analytical expressions, a universal numerical solution for an arbitrary continuous optimization objective is proposed based on a constrained numerical minimum search [30], and the procedure is depicted in Fig. 10.

In Fig. 10, the optimization procedure starts from the optimal control coordinate table $\boldsymbol{C}(\mathbf{X})$, constraint condition $\boldsymbol{B}(\mathbf{X})$ for operation region conditions and the ZVS conditions (if ZVS operation is also considered, the ZVS conditions are added to the constraint condition $\boldsymbol{B}(\mathbf{X})$. Noted that when the ZVS conditions are considered, the regions will shrink, and this impact will be analyzed in Section IV -E), the predefined range of M and P, the expression of optimization objective $\boldsymbol{A}(\mathbf{X})$, and the iteration of M and P, denoted as dM and dP. Then, it iterates through the whole predefined operating range. As for the optimization control coordinate $\mathbf{X_{opt}}$, there are two ways to calculate them. The first one is the direct calculation of control coordinate with boundary conditions (denoted as $\mathbf{X_{opt\text{-}B}}$), and the second one is the tangent point searching method introduced in Section III (denoted as $\mathbf{X_{opt\text{-}i}}$, where i is the number of region). When the

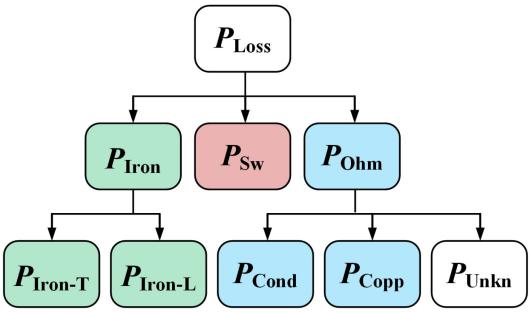

Fig. 11. Power loss breakdown of a DAB converter.

tangent point is located in the feasible region (i.e., $\boldsymbol{B}(\mathbf{X_{opt\text{-}i}}) \leq 0$), the $\mathrm{EF_i}$ is set to 1. Otherwise, the exit flag is reset to 0. Noted that when the ZVS constraint is taken into consideration, the alternative operation regions are expanded from regions 1–3 to all regions. After traversing all regions, if there exist at least one $\mathrm{EF_i} = 1$, the optimal control coordinate is found as $\mathbf{X_{opt\text{-}i}}$. Otherwise, the optimal control coordinate is found as $\mathbf{X_{opt\text{-}B}}$. Repeat the abovementioned process until M and P traverse through all the predefined range of M and P, and the optimal control coordinate in the whole operation range in obtained.

E. Efficiency-Oriented Optimization Objective Design for DAB

The total power loss breakdown of a DAB converter P_{Loss} is depicted in Fig. 11. The conduction loss P_{Cond} is related to I_{rms} while P_{SW} is related to I_{Peak}, and also the value of i_{L} at switching instants. P_{Iron} is divided into the iron loss of the inductor $P_{\mathrm{Iron\text{-}L}}$ and the iron loss of the transformer $P_{\mathrm{Iron\text{-}T}}$. P_{Unkn} is majorly related to the temperature dependent conduction loss of the power switches [31].

The core loss density is usually provided by the datasheet for sinusoidal flux density waveforms. $P_{\mathrm{Iron\text{-}L}}$ and $P_{\mathrm{Iron\text{-}T}}$ can be roughly estimated by the original Steinmetz equation

$$P_{\mathrm{Iron-L}} = P_{\mathrm{VL}} V_{\mathrm{eL}} = k_{\mathrm{L}} f_{\mathrm{s}}^{\alpha_{\mathrm{L}}} B_{\mathrm{Lm}}^{\beta_{\mathrm{L}}}.$$
$$P_{\mathrm{Iron-T}} = P_{\mathrm{VT}} V_{\mathrm{eT}} = k_{\mathrm{T}} f_{\mathrm{s}}^{\alpha_{\mathrm{T}}} B_{\mathrm{Tm}}^{\beta_{\mathrm{T}}}. \tag{37}$$

where P_{VL}, P_{VT}, V_{eL}, V_{eT}, B_{Lm}, and B_{Tm} are the core loss densities, core volumes, and magnetic flux density amplitudes of the inductor and the transformer, k_{L}, α_{L}, β_{L}, and k_{T}, α_{T}, β_{T} are the Steinmetz parameters.

According to the Faraday's law, we have

$$v_{\mathrm{CD}}(\theta) = N_{\mathrm{T}} A_{\mathrm{cT}} \frac{dB_{\mathrm{T}}(\theta)}{d\theta}; v_{\mathrm{L}}(\theta) = N_{\mathrm{L}} A_{\mathrm{cL}} \frac{dB_{\mathrm{L}}(\theta)}{d\theta} \tag{38}$$

where N_{T}, N_{L}, A_{cT}, and A_{cL} are the number of the winding turns, and the effective core cross section of the inductor and the transformer.

Hence, the relation of B_{Lm} and B_{Tm} with peak current I_{Peak} can be expressed as

$$B_{\mathrm{Lm}} \propto I_{\mathrm{Peak}}; B_{\mathrm{Tm}} \propto I_{\mathrm{Peak}}. \tag{39}$$

The major part of the switching loss P_{SW} in the DAB is caused by the MOSFETs with I_{Peak} turn-OFF current [31]. Hence, P_{SW} can be roughly calculated as

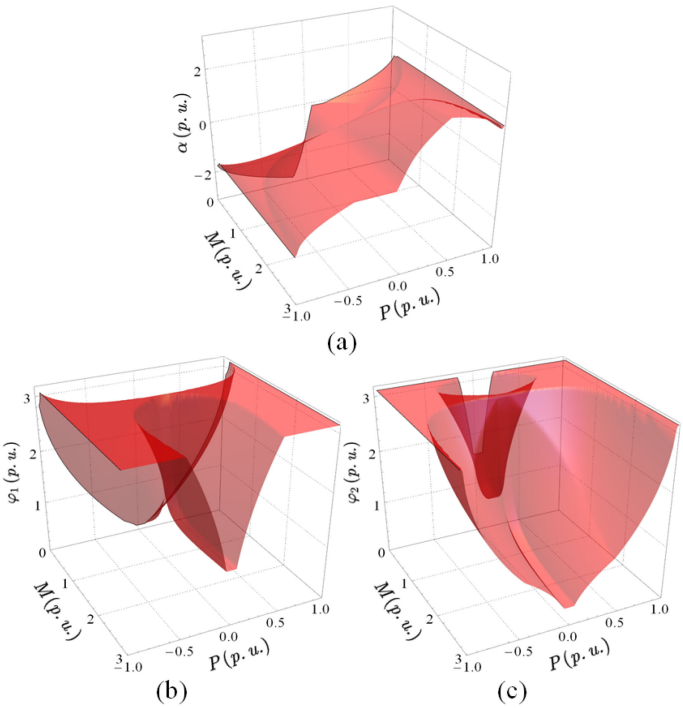

Fig. 12. (a) Optimal surface α of when $P_{\mathrm{Loss}} = A(\mathbf{X})$. (b) Optimal surface of φ_1 when $P_{\mathrm{Loss}} = A(\mathbf{X})$. (c) Optimal surface of φ_2 when $P_{\mathrm{Loss}} = A(\mathbf{X})$.

$$P_{\mathrm{SW}} \approx \frac{I_{\mathrm{Peak}}^2}{48 C_{\mathrm{ds}} f_{\mathrm{s}}}. \tag{40}$$

Consequently, the overall power loss of a DAB, P_{Loss} can be expressed as

$$\begin{aligned} P_{\mathrm{Loss}} &= P_{\mathrm{SW}} + P_{\mathrm{Iron-L}} + P_{\mathrm{Iron-T}} + P_{\mathrm{Cond}} + P_{\mathrm{Copp}} + P_{\mathrm{Unkn}} \\ &\approx K_{\mathrm{A}} \left(K_{\mathrm{L}} I_{\mathrm{Peak}}^{\beta_{\mathrm{L}}} + K_{\mathrm{T}} I_{\mathrm{Peak}}^{\beta_{\mathrm{T}}} + K_{\mathrm{SW}} I_{\mathrm{Peak}}^2 + K_{\mathrm{Cond}} I_{\mathrm{rms}}^2 \right) \end{aligned} \tag{41}$$

where K_{A}, K_{L}, K_{T}, K_{SW}, and K_{Cond} are the coefficients with $K_{\mathrm{L}} + K_{\mathrm{T}} + K_{\mathrm{SW}} + K_{\mathrm{Cond}} = 1$.

P_{Loss} can be regarded as the optimization objective of the control coordinate, and we can also obtain the control coordinate table $C(\mathbf{X})$ when $P_{\mathrm{Loss}} = A(\mathbf{X})$. For example, when $\beta_{\mathrm{L}} = \beta_{\mathrm{T}} = 2.5$, $K_{\mathrm{L}} = 0.05$, $K_{\mathrm{T}} = 0.05$, $K_{\mathrm{SW}} = 0.3$, and $K_{\mathrm{Cond}} = 0.6$, the surface of the optimal control coordinate (α, φ_1, φ_2) with the change of M and P is depicted in Fig. 12.

As can be observed from Fig. 12, it is better to fit the surfaces of α, φ_1, and φ_2 into piecewise functions. Due to the symmetric characteristic of DAB, only regions 1–3 are required to be fitted. Because the control coordinate with minimum I_{Peak} and minimum I_{rms} are identical in the low and high power regions, the control coordinate with $P_{\mathrm{Loss}} = A(\mathbf{X})$ is also identical in these regions. In medium power region, there is $\varphi_2 = \pi$ when $M < 1$.

The fitted surfaces of α and φ_1 together with the original data points are depicted in Fig. 13.

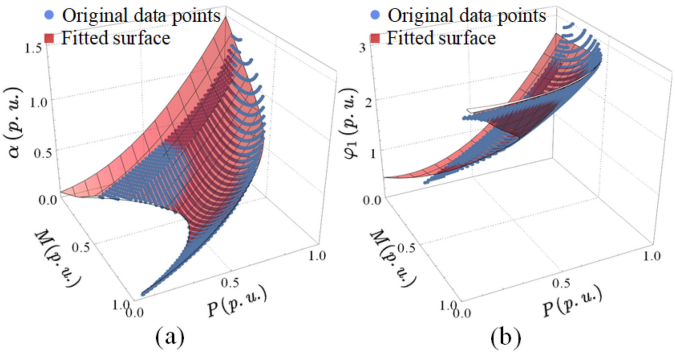

Fig. 13. (a) Fitted surface of α in medium power regions when $P_{\mathrm{Loss}} = A(\mathbf{X})$. (b) Fitted surface of φ_1 in medium power regions when $P_{\mathrm{Loss}} = A(\mathbf{X})$.

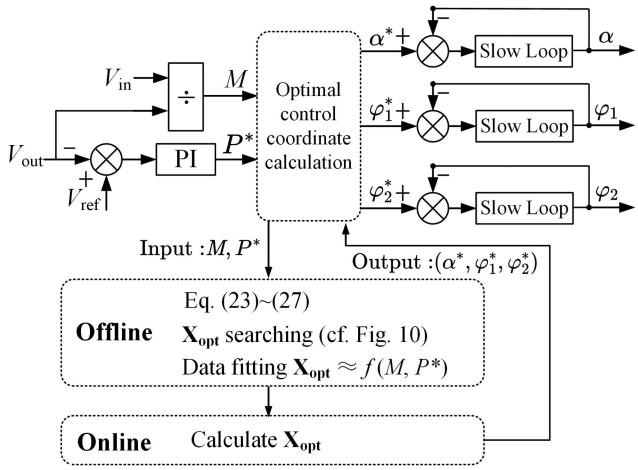

Fig. 14. Optimal control coordinate calculation of DAB, including the offline optimal control coordinate searching, offline data fitting, and online calculation.

The fitted functions of α and φ_1 are given as

$$\begin{aligned}\alpha\,(M,P) &\approx 2.02M^2 - 2.03M + 1.18P^2 + 0.25P + 0.06MP\\ \varphi_1\,(M,P) &\approx 2.40M^2 + 0.66M + 2.94P^2 - 0.72P + 0.44MP.\end{aligned} \tag{42}$$

With the offline optimal control coordinate determination and polynomial control coordinate data fitting, the fitted functions of α and φ_1 can be embedded to the online digital control of DAB. As depicted in Fig. 14, the control coordinate reference (α^*, $\varphi_1{}^*$, $\varphi_2{}^*$) can be calculated from P^* and M.

To eliminate the fast changing control coordinate reference, a slow loop is used to slow down the change of control coordinate reference. After obtaining (α^*, $\varphi_1{}^*$, $\varphi_2{}^*$), the gate signal generation block determines when to activate the turn-ON signals for the corresponding switches of the DAB converter.

It has to be mentioned that the abovementioned ZVS region analysis is based on the ideal lossless model of DAB, the charging and discharging processes of the switches parasitic capacitors during deadtime are neglected. Actually, the modulation schemes with minimum I_{rms} and I_{Peak} in low power regions are only with theoretical instead of practical ZVS capability, which resulted in increased switching loss. Two examples with $P = 0.1$, $M = 1.4$ are depicted in Fig. 15 to illustrate this phenomenon.

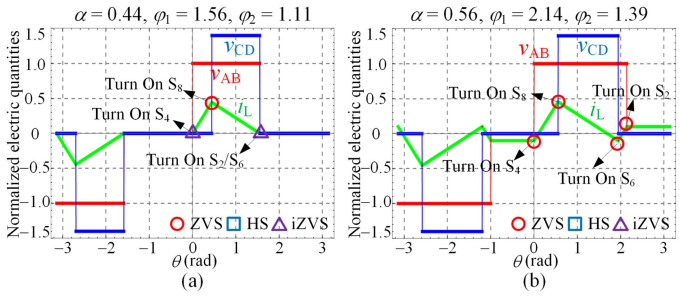

Fig. 15. Operation waveforms with (a) minimum I_{rms} and I_{Peak} modulation scheme with ($\alpha = 0.44$, $\varphi_1 = 1.56$, $\varphi_2 = 1.11$). (b) Full-ZVS modulation scheme with ($\alpha = 0.56$, $\varphi_1 = 2.14$, $\varphi_2 = 1.39$).

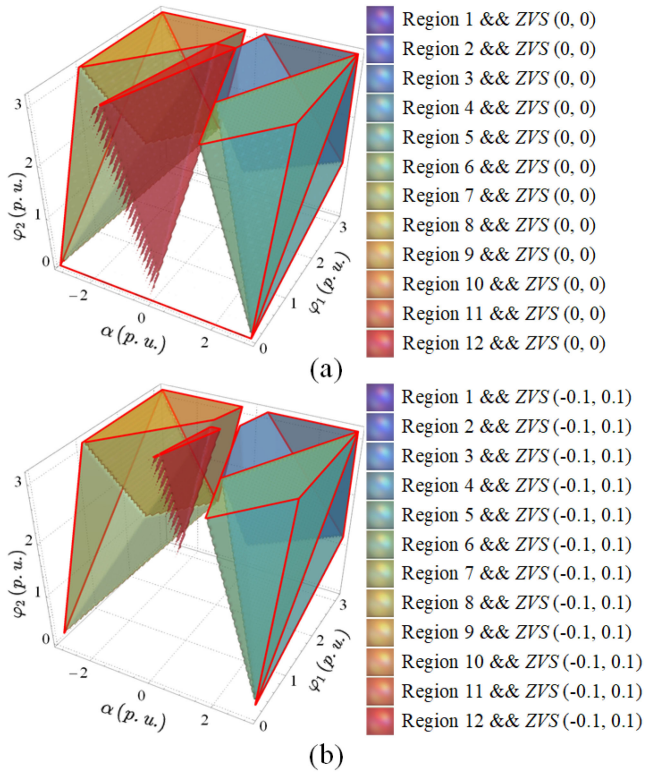

Fig. 16. Feasible regions with (a) ZVS (0, 0). (b) ZVS (–0.1, 0.1) when $M = 0.8$.

In Fig. 15(a), the control coordinate is with minimum I_{rms} and I_{Peak}. However, the turning on of S_2, S_4, and S_6 are with zero current, which is not sufficient to fully discharge the parasitic capacitors of the S_1, S_3, and S_5. This process is termed as iZVS. The capacitive energy across the switches is dissipated, result in increased P_{SW} [28]. In Fig. 15(b), the ZVS of all primary and secondary switches are realized at the cost of a higher I_{rms}, and I_{Peak}. Because there is $P << 1$ in this condition, P_{SW} only accounts for a small fraction of the total loss, the efficiency in Fig. 16(b) is higher than that in Fig. 16(a) in practice (cf., the efficiency curves in Fig. 21 and the ZVS conditions in Fig. 22). Hence, the ZVS constraint should be reevaluated. The ZVS constraint is denoted as ZVS (I_{P}, I_{N}), where I_{P} and I_{N} are the normalized minimum currents for ZVS of primary and secondary switches. To achieve ZVS of primary and secondary

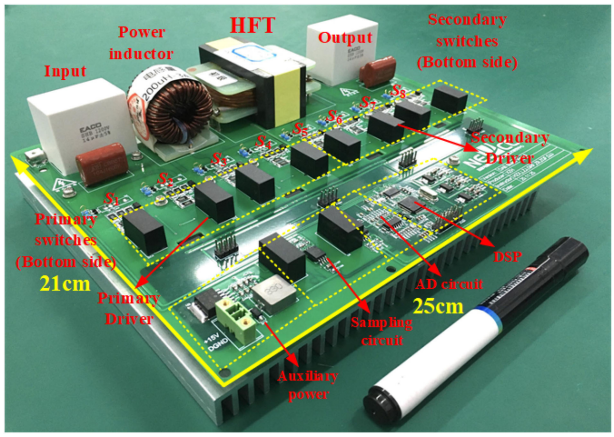

Fig. 17. Prototype of the DAB converter.

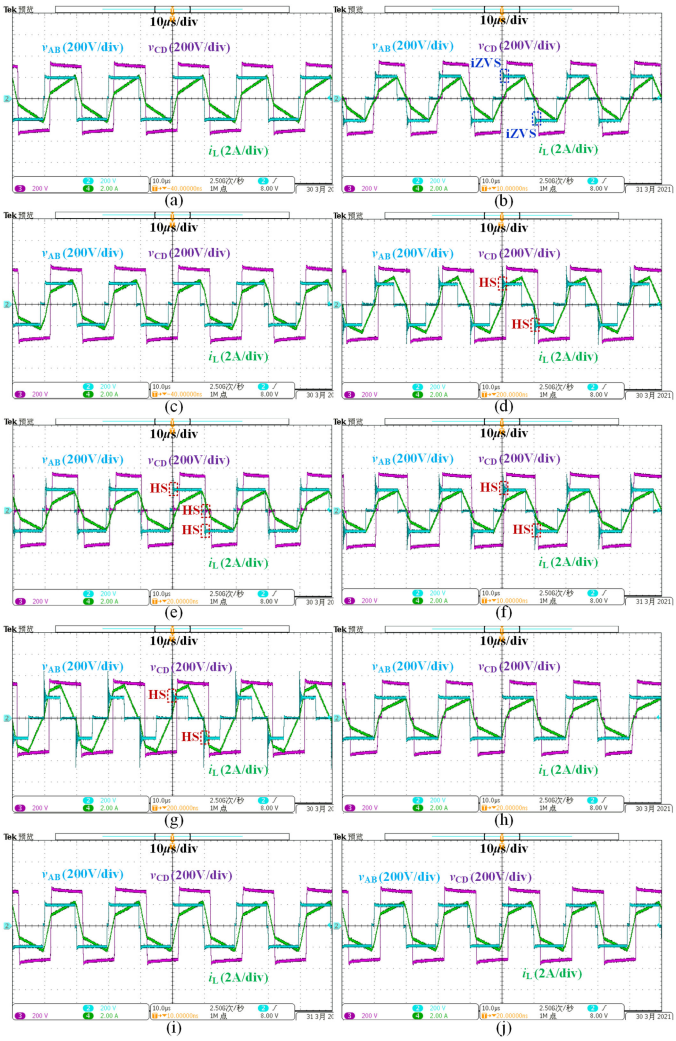

Fig. 18. Operation waveforms when $V_{\rm in} = 200$ V, $V_{\rm out} = 320$ V ($M = 0.8$). (a) Minimum $I_{\rm rms}$. (b) Minimum $V_{\rm rms}$. (c) Minimum $I_{\rm Peak}$. (d) Minimum $S_{\rm AB}$. (e) Minimum $S_{\rm CD}$. (f) Minimum $S_{\rm AB}$ $S_{\rm CD}$. (g) Minimum $|Q_{\rm AB}|$. (h) Minimum $|Q_{\rm CD}|$. (i) Minimum $|Q_{\rm AB}| + |Q_{\rm CD}|$. (j) Minimum $P_{\rm Loss} = A(\mathbf{X})$ modulation schemes. (Ch2: the input voltage of the HFT $v_{\rm AB}$, 200 V/div; Ch3: the output voltage of the HFT $v_{\rm CD}$, 200 V/div; Ch4: the inductor current $i_{\rm L}$, 2 A/div).

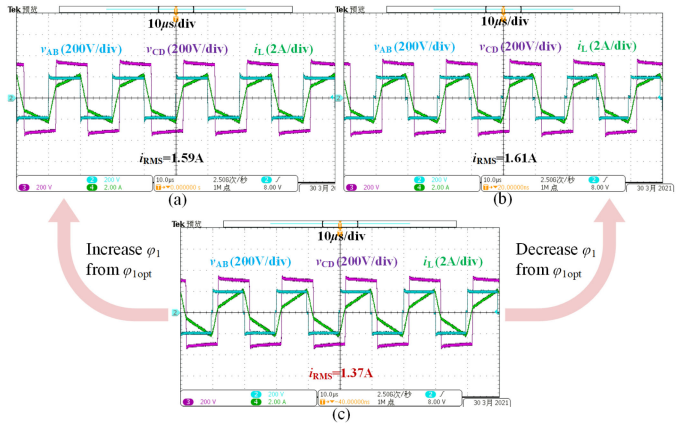

Fig. 19. Operation waveforms with minimum $I_{\rm rms}$ when $V_{\rm in} = 200$ V, $V_{\rm out} = 320$ V. (a) When $\varphi_1 < \varphi_{1\rm opt}$. (b) When $\varphi_1 = \varphi_{1\rm opt}$. (c) When $\varphi_1 > \varphi_{1\rm opt}$. (Ch2: the input voltage of the HFT $v_{\rm AB}$, 200 V/div; Ch3: the output voltage of the HFT $v_{\rm CD}$, 200 V/div; Ch4: the inductor current $i_{\rm L}$, 2 A/div).

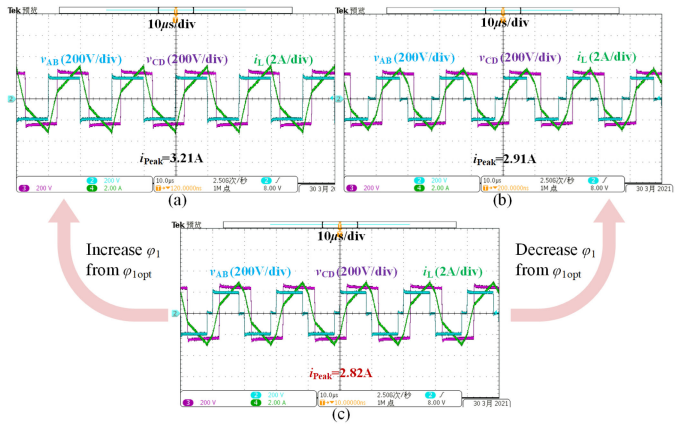

Fig. 20. Operation waveforms with minimum $I_{\rm Peak}$ when $V_{\rm in} = 200$ V, $V_{\rm out} = 240$ V. (a) When $\varphi_1 < \varphi_{1\rm opt}$. (b) When $\varphi_1 = \varphi_{1\rm opt}$. (c) When $\varphi_1 > \varphi_{1\rm opt}$. (Ch2: the input voltage of the HFT $v_{\rm AB}$, 200 V/div; Ch3: the output voltage of the HFT $v_{\rm CD}$, 200 V/div; Ch4: the inductor current $i_{\rm L}$, 2 A/div).

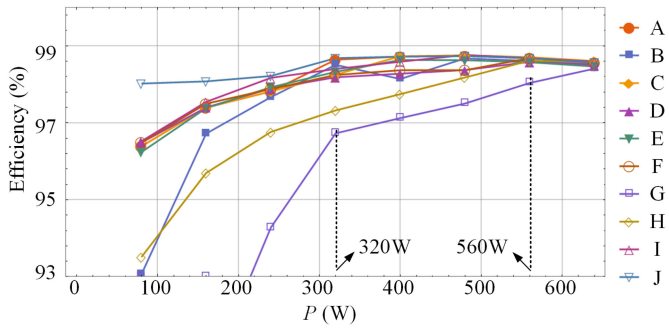

A: Minimum $I_{\rm RMS}$; B: Minimum $V_{\rm RMS}$; C: Minimum $S_{\rm AB}$; D: Minimum $S_{\rm CD}$; E: Minimum $S_{\rm AB}$ $S_{\rm CD}$; F: Minimum $I_{\rm Peak}$; G: Minimum $|Q_{\rm AB}|$; H: Minimum $|Q_{\rm CD}|$; I: Minimum $|Q_{\rm AB}| + |Q_{\rm CD}|$; J: Minimum $P_{\rm Loss}$.

Fig. 21. Efficiency curves of multiple modulation schemes when $V_{\rm in} = 200$ V, $V_{\rm out} = 320$ V.

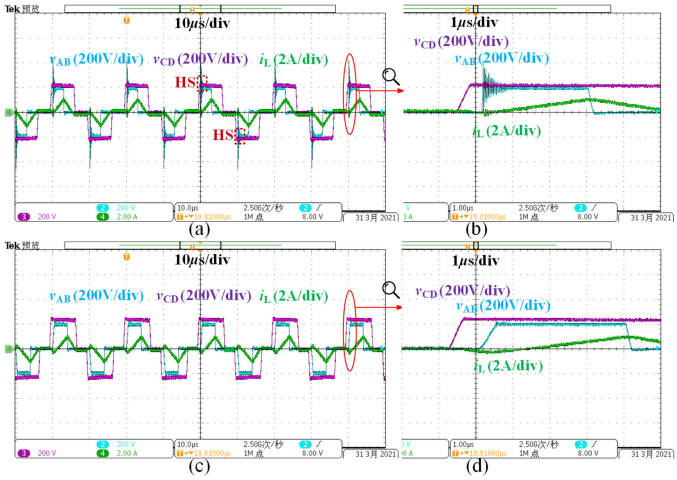

Fig. 22. (a) Operation waveforms considering the ideal ZVS. (b) Detailed switching process of the ideal ZVS. (c) Operation waveforms considering the actual ZVS. (d) Detailed switching process of the actual ZVS. (Ch2: the input voltage of the HFT v_{AB}, 200 V/div; Ch3: the output voltage of the HFT v_{CD}, 200 V/div; Ch4: the inductor current i_L, 2 A/div).

TABLE IV
SPECIFICATION OF THE EXPERIMENTAL PROTOTYPE

Component	Part number	Parameters
MOSFETs	C2M0080170P × 8	1.7 kV, 40 A, 80 mΩ
MCU	TMS320F28062	Digital signal processer C2000 32-bit 90-MHz
Power inductor	Permalloy core	200 μH, 50 kHz
HFT	1:2 turn ratio, PC95/EEP70B	$L_{lk} \approx 2.86$ μH, $L_m \approx 500$ μH.

switches, I_P should be greater than a certain positive number while I_N should be smaller than a certain negative number. These numbers can be calculated through the current based, or energy based ZVS analysis [30], and the detailed process is not expanded in this article. Feasible regions with ZVS (0, 0), and ZVS (−0.1, 0.1) when $M = 0.8$ are depicted in Fig. 16.

With the increasing of $|I_P|$ and $|I_N|$, the range of feasible regions shrink. When the tangent point is out of the feasible region with ZVS (−0.1, 0.1), the suboptimal control coordinate can be selected at the ZVS boundary.

V. EXPERIMENTAL RESULT

The experimental results of multiple modulation schemes are presented in this section with a laboratory prototype depicted in Fig. 17 and the basic technical data of the prototype are listed in Table IV. The switching frequency is 50 kHz, the input voltage is 200 V, and the output voltage varies from 240–320 V. Due to the symmetric characteristic of DAB, the presented experimental result only contains the step-down condition with positive power transmission.

TABLE V
EXPRESSIONS OF POWER TRANSMISSION IN DIFFERENT REGIONS

Region	Power transmission
1	$\frac{2\varphi_2(2\alpha-\varphi_1+\varphi_2)}{\pi^2}$
2	$\frac{2\varphi_1\varphi_2-2(\varphi_1-\alpha)^2}{\pi^2}$
3	$\frac{-2(\pi^2+\varphi_1^2+\varphi_2^2+2\alpha^2)+2\varphi_1\varphi_2+4\pi(\alpha+\varphi_2)+4\alpha(\varphi_1-\varphi_2)}{\pi^2}$
4	$\frac{2\varphi_1\varphi_2}{\pi^2}$
5	$\frac{2\varphi_2(2\pi-2\alpha+\varphi_1)-2\varphi_2^2-2(\pi-\alpha)^2}{\pi^2}$
6	$\frac{2\varphi_1(2\pi-2\alpha+\varphi_1-\varphi_2)}{\pi^2}$
7	$\frac{-2\varphi_2(2\pi+2\alpha-\varphi_1+\varphi_2)}{\pi^2}$
8	$\frac{2(\varphi_1-\pi-\alpha)^2-2\varphi_1\varphi_2}{\pi^2}$
9	$\frac{2(\pi^2+\varphi_1^2+\varphi_2^2+2\alpha^2)-2\varphi_1\varphi_2+4\pi(\alpha-\varphi_1)-4\alpha(\varphi_1-\varphi_2)}{\pi^2}$
10	$\frac{-2\varphi_1\varphi_2}{\pi^2}$
11	$\frac{2\alpha^2+2\varphi_2(2\alpha-\varphi_1)+2\varphi_2^2}{\pi^2}$
12	$\frac{2\varphi_1(2\alpha-\varphi_1+\varphi_2)}{\pi^2}$

A. Comparison of Multiple Modulation Schemes

Operation waveforms with minimum I_{rms}, minimum V_{rms}, minimum I_{Peak}, minimum S_{AB}, minimum S_{CD}, minimum S_{AB} S_{CD}, minimum $|Q_{AB}|$, minimum $|Q_{CD}|$, minimum $|Q_{AB}| + |Q_{CD}|$, and minimum $P_{Loss} = A(\mathbf{X})$ modulation schemes mentioned previously are depicted in Fig. 18. In Fig. 18, the input, output voltage are fixed at $V_{in} = 200$ V, $V_{out} = 320$ V ($M = 0.8$), and the output power is 280 W. In this case, the base values of voltage V_{Base}, current I_{Base}, and power P_{Base} are given as $V_{Base} = 200$ V, $I_{Base} = 3.18$ A, $P_{Base} = 636$ W (also the base value of apparent power S_{AB}/S_{CD} 636 VA, and the base value of reactive power Q_{AB}/Q_{CD} 636 Var). The blue line denotes the input port voltage v_{AB} (200 V/div), the purple line denotes the output port voltage v_{CD} (200 V/div), and the green line denotes the inductor current i_L (2 A/div).

To validate the correctness of the global optimal minimum, two cases when I_{rms} and I_{Peak} are chosen as the optimization objective are studied. The operation waveforms when φ_1 is smaller or greater than the optimal value of φ_1, φ_{1opt}, are depicted in Figs. 19 and 20. When φ_1 is changed, α is also adjusted to ensure the identical power transmission. When φ_1 is greater or smaller than φ_{1opt}, I_{rms}, and I_{Peak} both increase, which verified the correctness of the global optimal minimum.

B. Efficiency Curves of Multiple Modulation Schemes

The efficiency curves of multiple modulation schemes mentioned previously when $V_{in} = 200$ V, $V_{out} = 320$ V, output power

TABLE VI
EXPRESSIONS OF I_{RMS} IN DIFFERENT REGIONS

Region	I_{RMS}
1	$\sqrt{\frac{(3\pi-2\varphi_2)\varphi_1^2+2M^2\left(6\pi-\varphi_1^3\right)+2M\varphi_2\left(6\alpha^2-3\pi\varphi_1+3\varphi 1^2-3\varphi_1\varphi_2+2\varphi_1^2+6\alpha(\varphi_2-\varphi_1)\right)}{12\pi}}$
2	$\sqrt{\frac{(3\pi-2\varphi_1)\varphi_1^2+M^2(3\pi-2\varphi_2)\varphi_2^2-4M(\alpha-\varphi_1)^3-6M\varphi_1\varphi_2(\pi-2\alpha+\varphi_1-\varphi_2)}{12\pi}}$
3	$\sqrt{\frac{(3\pi-2\varphi_1)\varphi_1^2+M^2(3\pi-2\varphi_2)\varphi_2^2+2M(\pi-2\alpha+\varphi_1-\varphi_2)\left(2\left(\pi^2+\alpha^2-\alpha\varphi_1+\varphi_1^2-\pi(\alpha+\varphi_1)\right)-\varphi_2(4\pi-2\alpha+\varphi_1)+2\varphi_2^2\right)}{12\pi}}$
4	$\sqrt{\frac{3\pi(\varphi_1-M\varphi_2)^2-2M^2\varphi_2^3-2\left(\varphi_1^3+3M\varphi_1\varphi_2(\varphi_1-2\alpha-\varphi_2)\right)}{12\pi}}$
5	$\sqrt{\frac{(3\pi-2\varphi_1)\varphi_1^2+M\left(\begin{matrix}4(\pi-\alpha)^3-6\varphi_2\left(2(\pi-\alpha)^2+(\pi-2\alpha)\varphi_1+\varphi_1^2\right)\\+6\left((2+3M)\pi-2\alpha+\varphi_1\right)\varphi_2^2-2(2+M)\varphi_2^3\end{matrix}\right)}{12\pi}}$
6	$\sqrt{\frac{(3\pi-2\varphi_1)\varphi_1^2+M^2(3\pi-2\varphi_2)\varphi_2^2-2M\varphi_1\left(6(\pi-\alpha)(\pi-\alpha+\varphi_1)+2\varphi_1^2-3\varphi_2(3\pi-2\alpha+\varphi_1-\varphi_2)\right)}{12\pi}}$
7	$\sqrt{\frac{(3\pi-2\varphi_1)\varphi_1^2-6M\varphi_2\left(2(\pi+\alpha)^2-(3\pi+2\alpha)\varphi_1+\varphi_1^2\right)+3M\left((M-4)\pi-4\alpha+2\varphi_1\right)\varphi_2^2-2M(M+2)\varphi_2^3}{12\pi}}$
8	$\sqrt{\frac{(3\pi-2\varphi_1)\varphi_1^2+M^2(3\pi-2\varphi_2)\varphi_2^2+4M(\pi+\alpha-\varphi_1)^3-6M\varphi_1\varphi_2(\pi+2\alpha-\varphi_1-\varphi_2)}{12\pi}}$
9	$\sqrt{\frac{(3\pi-2\varphi_1)\varphi_1^2+M^2(3\pi-2\varphi_2)\varphi_2^2+2M(\pi+2\alpha-\varphi_1+\varphi_2)\left(2\left(\pi^2+\pi\alpha+\alpha^2-(2\pi+\alpha)\varphi_1+\varphi_1^2\right)-(2\pi-2\alpha+\varphi_1)\varphi_2+2\varphi_2^2\right)}{12\pi}}$
10	$\sqrt{\frac{3\pi(\varphi_1-M\varphi_2)^2-2M^2\varphi_2^3-2\left(\varphi_1^3+3M\varphi_1\varphi_2(2\alpha+\varphi_2-\varphi_1)\right)}{12\pi}}$
11	$\sqrt{\frac{(3\pi-2\varphi_1)\varphi_1^2+M\left(\begin{matrix}4\alpha^3+6\varphi_2\left(2\alpha^2-(\pi+2\alpha)\varphi_1+\varphi_1^2\right)\\+3(M\pi+4\alpha-2\varphi_1)\varphi_2^2-2(M-2)\varphi_2^3\end{matrix}\right)}{12\pi}}$
12	$\sqrt{\frac{(3\pi-2\varphi_1)\varphi_1^2+M^2(3\pi-2\varphi_2)\varphi_2^2+2M\varphi_1\left(6\alpha(\alpha+\varphi_2-\varphi_1)+2\varphi_1^2-3\varphi_2(\pi+\varphi_1-\varphi_2)\right)}{12\pi}}$

ranged from 80–640 W are depicted in Fig. 21. For various output power conditions, the efficiency with $A(\mathbf{X})$ is higher than the other modulation schemes for most of the operation points, especially in low power conditions. When the power transmission is 80 W, the efficiency of $A(\mathbf{X})$ is 97.9%, which is 1.4% higher than the minimum I_{rms} and minimum I_{Peak} modulation schemes. As for minimum $|Q_{\mathrm{AB}}|$ or minimum $|Q_{\mathrm{CD}}|$ modulation schemes, the efficiencies are the lowest almost in the whole power range. This is because there is $|Q_{\mathrm{AB}}|=0$ when $P<$ 320 W, and $|Q_{\mathrm{CD}}|=0$ when $P<560$ W [see Figs. 15(g), (h), and 21]. To achieve $|Q_{\mathrm{AB}}|=0$ or $|Q_{\mathrm{CD}}|=0$, the ZVS implementation as well as all other electric quantities have to deteriorate, which resulted in low efficiency.

C. Optimization Considering the Actual ZVS Condition

As for the modulation schemes with minimum I_{RMS}, I_{Peak}, S_{AB}, and S_{CD}, although all switches are without HS, the inductor current at the switching instant is insufficient to implement full ZVS. When considering the actual ZVS process, $|I_{\mathrm{P}}|$ and $|I_{\mathrm{N}}|$ are chosen as 0.1 p.u. according to the parasitic capacitors of the MOSFETs. When ZVS $(-0.1, 0.1)$ is applied to the optimal control coordinate calculation algorithm in Fig. 10, only the $\mathbf{X_{opt}}$ in the low power region is affected. On the other hand, the $\mathbf{X_{opt}}$ exhibits a step change (from region 12 to region 5) when 160 W $< P <$ 320 W due to the ZVS constraints. To achieve a smooth transition (from region 12 to region 1), $|I_{\mathrm{P}}|$ and $|I_{\mathrm{N}}|$ decrease linearly, which caused increased P_{SW} and efficiency deterioration.

Two typical operation waveforms considering the ideal ZVS and the actual ZVS are depicted in Fig. 22. The achievement of the actual ZVS is at the cost of an increased I_{rms} and I_{Peak}.

On combining the abovementioned experiments, the conclusions can be drawn.

1) As for the optimization objective with port AB (S_{AB}, $|Q_{\mathrm{AB}}|$), φ_1 is usually reduced to obtain a smaller value of the objective function. Similar conclusions can also be drawn for the optimization objective with port CD. In contrast, global electric quantities (I_{rms}, V_{rms}, and I_{Peak}) or the optimization objective considering both port AB and port CD (S_{AB} S_{CD}, $|Q_{\mathrm{AB}}|+|Q_{\mathrm{CD}}|$) are with better adaptability or versatility (closer control coordinate and better overall average efficiency).
2) The optimization objective with port AB or port CD is more likely to cause a sharp deterioration of other electric quantities, which is especially noticeable in low power conditions.
3) A small φ_1/φ_2 will be detrimental to the ZVS of primary/secondary switches, e.g., the ZVS for primary switches for minimum S_{AB} or $|Q_{\mathrm{AB}}|$ is difficult compared to minimum I_{rms} or S_{AB}.
4) When considering actual ZVS, the achievement of the actual ZVS (reduced P_{SW}) is at the cost of an increased P_{Cond}.

VI. CONCLUSION

Because of the nonconvex feasible region and nonconvex operation objectives of DAB, regular convex methods are ineffective in the optimization of DAB. To solve these problems, a unified description method both suitable in time and frequency domain is proposed based on the standard decomposition of instantaneous electric quantities. Besides, a unified optimization method is proposed based on tangent point searching for the feasible region and optimization objective surfaces. With these two methods, the optimization objective can be designed arbitrarily. An efficiency-oriented optimization objective design method and a universal numerical solution for an arbitrary continuous optimization objective are proposed considering all electric quantities as well as the ZVS conditions. The experimental results proved the effectiveness of the design method, and the efficiency is greatly improved compared to the conventional and recently published modulation schemes.

APPENDIX

The expressions of power transmission, and I_{rms} in regions 1–12 are summarized in Tables V and VI.

REFERENCES

[1] Z. Zhang, Y. Cai, Y. Zhang, D. Gu, and Y. Liu, "A distributed architecture based on microbank modules with self-reconfiguration control to improve the energy efficiency in the battery energy storage system," *IEEE Trans. Power Electron.*, vol. 31, no. 1, pp. 304–317, Jan. 2016.

[2] B. Zhao, Q. Song, and W. Liu, "A practical solution of high-frequency-link bidirectional solid-state transformer based on advanced components in hybrid microgrid," *IEEE Trans. Ind. Electron.*, vol. 62, no. 7, pp. 4587–4597, Jul. 2015.

[3] Q. Ye, R. Mo, and H. Li, "Low-frequency resonance suppression of a dual-active-bridge DC/DC converter enabled DC microgrid," *IEEE J. Emerg. Sel. Topics Power Electron.*, vol. 5, no. 3, pp. 982–994, Sep. 2017.

[4] L. Wang, D. Zhang, Y. Wang, B. Wu, and H. S. Athab, "Power and voltage balance control of a novel three-phase solid-state transformer using multilevel cascaded H-Bridge inverters for microgrid applications," *IEEE Trans. Power Electron.*, vol. 31, no. 4, pp. 3289–3301, Apr. 2016.

[5] F. Krismer and J. W. Kolar, "Accurate small-signal model for the digital control of an automotive bidirectional dual active bridge," *IEEE Trans. Power Electron.*, vol. 24, no. 12, pp. 2756–2768, Dec. 2009.

[6] F. Krismer and J. W. Kolar, "Efficiency-optimized high-current dual active bridge converter for automotive applications," *IEEE Trans. Ind. Electron.*, vol. 59, no. 7, pp. 2745–2760, Jul. 2012.

[7] B. Zhao, Q. Song, J. Li, W. Liu, G. Liu, and Y. Zhao, "High-frequency-link DC transformer based on switched capacitor for medium-voltage DC power distribution application," *IEEE Trans. Power Electron.*, vol. 31, no. 7, pp. 4766–4777, Jul. 2016.

[8] T. Zhao, G. Wang, S. Bhattacharya, and A. Q. Huang, "Voltage and power balance control for a cascaded H-Bridge converter-based solid-state transformer," *IEEE Trans. Power Electron.*, vol. 28, no. 4, pp. 1523–1532, Apr. 2013.

[9] L. Wang, D. Zhang, Y. Wang, B. Wu, and H. S. Athab, "Power and voltage balance control of a novel three-phase solid-state transformer using multilevel cascaded H-Bridge inverters for microgrid applications," *IEEE Trans. Power Electron.*, vol. 31, no. 4, pp. 3289–3301, Apr. 2016.

[10] H. Shi *et al.*, "Minimum-backflow-power scheme of DAB-based solid-state transformer with extended-phase-shift control," *IEEE Trans. Ind. Appl.*, vol. 54, no. 4, pp. 3483–3496, Jul./Aug. 2018.

[11] J. Liu, J. Yang, J. Zhang, Z. Nan, and Q. Zheng, "Voltage balance control based on dual active bridge DC/DC converters in a power electronic traction transformer," *IEEE Trans. Power Electron.*, vol. 33, no. 2, pp. 1696–1714, Feb. 2018.

[12] X. Yu, X. She, X. Zhou, and A. Q. Huang, "Power management for DC microgrid enabled by solid-state transformer," *IEEE Trans. Smart Grid*, vol. 5, no. 2, pp. 954–965, Mar. 2014.

[13] R. W. DeDoncker, D. M. Divan, and M. H. Kheraluwala, "A three-phase soft-switched high power density DC-to-DC converter for high power applications," *IEEE Trans. Ind. Appl.*, vol. 27, no. 1, pp. 63–73, Jan./Feb. 1991.

[14] M. H. Kheraluwala, R. W. Gascoigne, D. M. Divan, and E. D. Baumann, "Performance characterization of a high-power dual active bridge DC-to-DC converter," *IEEE Trans. Ind. Appl.*, vol. 28, no. 6, pp. 1294–1301, Nov./Dec. 1992.

[15] Y. Wang, S. W. H. de Haan, and J. A. Ferreira, "Optimal operating ranges of three modulation methods in dual active bridge converters," in *Proc. 6th Int. Power Electron. Motion Control Conf.*, Wuhan, China, May 2009, pp. 1397–1401.

[16] G. G. Oggier, G. O. Garciía, and A. R. Oliva, "Modulation strategy to operate the dual active bridge DC–DC converter under soft switching in the whole operating range," *IEEE Trans. Power Electron.*, vol. 26, no. 4, pp. 1228–1236, Apr. 2011.

[17] H. Bai and C. Mi, "Eliminate reactive power and increase system efficiency of isolated bidirectional dual-active-bridge DC–DC converters using novel dual-phase-shift control," *IEEE Trans. Power Electron.*, vol. 23, no. 6, pp. 2905–2914, Nov. 2008.

[18] B. Zhao, Q. Song, and W. Liu, "Power characterization of isolated bidirectional dual-active-bridge DC–DC converter with dual-phase-shift control," *IEEE Trans. Power Electron.*, vol. 27, no. 9, pp. 4172–4176, Sep. 2012.

[19] B. Zhao, Q. Song, and W. Liu, "Efficiency characterization and optimization of isolated bidirectional DC–DC converter based on dual-phase-shift control for DC distribution application," *IEEE Trans. Power Electron.*, vol. 28, no. 4, pp. 1711–1727, Apr. 2013.

[20] B. Zhao, Q. Yu, and W. Sun, "Extended-phase-shift control of isolated bidirectional DC–DC converter for power distribution in microgrid," *IEEE Trans. Power Electron.*, vol. 27, no. 11, pp. 4667–4680, Nov. 2012.

[21] H. Shi *et al.*, "Minimum-Backflow-Power scheme of DAB-based solid-state transformer with extended-phase-shift control," *IEEE Trans. Ind. Appl.*, vol. 54, no. 4, pp. 3483–3496, Jul./Aug. 2018.

[22] Q. Gu, L. Yuan, J. Nie, J. Sun, and Z. Zhao, "Current stress minimization of dual-active-bridge DC–DC converter within the whole operating range," *IEEE J. Emerg. Sel. Topics Power Electron.*, vol. 7, no. 1, pp. 129–142, Mar. 2019.

[23] J. Huang, Y. Wang, Z. Li, and W. Lei, "Unified triple-phase-shift control to minimize current stress and achieve full soft-switching of isolated bidirectional DC–DC converter," *IEEE Trans. Ind. Electron.*, vol. 63, no. 7, pp. 4169–4179, Jul. 2016.

[24] Z. Xiao, Z. He, H. Wang, A. Luo, Z. Shuai, and J. M. Guerrero, "General high-frequency-link analysis and application of dual active bridge converters," *IEEE Trans. Power Electron.*, vol. 35, no. 8, pp. 8673–8688, Aug. 2020.

[25] N. Schibli, "Symmetrical multilevel converters with two quadrant dc–dc feeding," Ph.D. dissertation, Faculty Eng. Sci. Technol., Ecole Polytech. Federale de Lausanne, Lausanne, Switzerland, 2000.

[26] F. Krismer and J. W. Kolar, "Closed form solution for minimum conduction loss modulation of DAB converters," *IEEE Trans. Power Electron.*, vol. 27, no. 1, pp. 174–188, Jan. 2012.

[27] A. Tong, L. Hang, G. Li, X. Jiang, and S. Gao, "Modeling and analysis of a dual-active-bridge-isolated bidirectional DC/DC converter to minimize RMS current with whole operating range," *IEEE Trans. Power Electron.*, vol. 33, no. 6, pp. 5302–5316, Jun. 2018.

[28] W. Choi, K. Rho, and B. Cho, "Fundamental duty modulation of dual-active-bridge converter for wide-range operation," *IEEE Trans. Power Electron.*, vol. 31, no. 6, pp. 4048–4064, Jun. 2016.

[29] B. Zhao, Q. Song, W. Liu, G. Liu, and Y. Zhao, "Universal high-frequency-link characterization and practical fundamental-optimal strategy for dual-active-bridge DC-DC converter under PWM plus phase-shift control," *IEEE Trans. Power Electron.*, vol. 30, no. 12, pp. 6488–6494, Dec. 2015.

[30] J. Everts, F. Krismer, J. Van den Keybus, J. Driesen, and J. W. Kolar, "Optimal ZVS modulation of single-phase single-stage bidirectional DAB AC–DC converters," *IEEE Trans. Power Electron.*, vol. 29, no. 8, pp. 3954–3970, Aug. 2014.

[31] H. Akagi, T. Yamagishi, N. M. L. Tan, S.-I. Kinouchi, Y. Miyazaki, and M. Koyama, "Power-Loss breakdown of a 750-V 100-kW 20-kHz bidirectional isolated DC–DC converter using SiC-MOSFET/SBD dual modules," *IEEE Trans. Ind. Appl.*, vol. 51, no. 1, pp. 420–428, Jan./Feb. 2015.

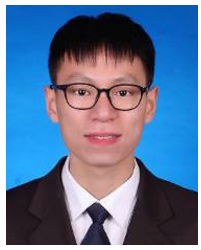

Ziheng Xiao (Student Member, IEEE) received the B.S. degree in electrical engineering and automation in 2017 from the College of Electrical and Information Engineering, Hunan University, Changsha, China, where he is currently working toward Ph.D. degree in electrical engineering.

His main research interests include the medium voltage dc system, dual active bridge converters, resonant converters, dc/dc converter series, parallel operation, and modular converter systems.

Zhixing He (Member, IEEE) was born in Hunan, China, 1989. He received the B.S. degree in information science and Engineering from Central South University, Changsha, China, in 2011, and the Ph.D. degree in electrical engineering from Hunan University, Changsha, China, in 2017.

He was with the Hunan University, as Postdoctoral Researcher between 2017 and 2018. He is currently an Associate Professor with the College of Electrical and Information Engineering, Hunan University, Changsha, China. His research interests include power electronics, medium voltage dc system, model predictive control, and modular multilevel converter.

Zongjian Li (Member, IEEE) received the B.S. degree in electronic information engineering from the College of engineering, Hunan Normal University, Changsha, China, in 2012, and the Ph.D. degree in electric engineering from Hunan University, Changsha, China, in 2020.

He is currently working as a Postdoctor with the College of Electrical and Information Engineering, Hunan University, Changsha, China. His research interests include Silicon Carbide power electronic devices and their applications in high voltage converter applications. His current research interests include the medium voltage dc system, resonant dc converter, and CC/CV dc/dc converters.

Lipeng Zhu (Member, IEEE) received the B.S. degree from the Huazhong University of Science and Technology, Wuhan, China, in 2012, the M.S. degree from Wuhan University, Wuhan, China, in 2015, and the Ph.D. degree from Tsinghua University, Beijing, China, in 2018, all in electrical engineering.

He was a Postdoctoral Fellow/Senior Research Assistant with The University of Hong Kong from 2018 to 2021. He is currently an Associate Professor with Hunan University. His research interests mainly include spatial-temporal energy data analysis, IoT data management and analytics in smart grids, synchrophasor measurement technologies, and data-driven power system stability and control.

Lei Wang (Senior Member, IEEE) received the B.Sc. degree in electrical and electronics engineering from the University of Macau (UM), Macao SAR, China, in 2011, the M.Sc. degree in electronics engineering from the Hong Kong University of Science and Technology, Hong Kong, in 2012, and the Ph.D. degree in electrical and computer engineering from UM, Macao, China, in 2017.

He was a Postdoctoral Fellow with the Power Electronics Laboratory, UM from Jan. 2017 to Feb. 2019. He was a Visiting Fellow with the Department of Electrical and Computer Engineering, University of Auckland, from Feb. 2019 to Aug. 2019. In 2019, he was with the College of Electrical and Information Engineering, Hunan University, Changsha, China, where he is currently a Full Professor. He has authored one Springer books, one Elsevier book chapter, five patents (U.S.A and China) and more than 70 journal and conference papers.

Dr. Wang was the recipient of the champion award in the "Schneider Electric Energy Efficiency Cup," Hong Kong, 2011, Macao Science and Technology R&D Award for Postgraduates (Ph.D) in 2018.